Edinburgh Research Explorer

Metamorphic olivine records external fluid infiltration during serpentinite dehydration
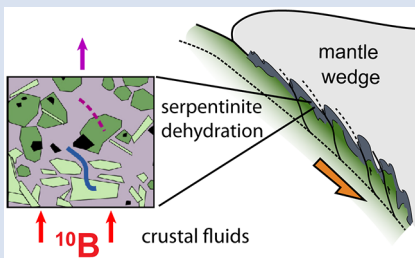
Metamorphic olivine records external fluid infiltration during serpentinite dehydration

E. Clarke[1], J.C.M. De Hoog[1*], L.A. Kirstein[1], J. Harvey[2], B. Debret[3]

OPEN ACCESS

Abstract

doi: 10.7185/geochemlet.2039

We used boron (B) isotope systematics of co-existing olivine and serpentine to study deep fluid flow in subduction zones. Metamorphic olivine produced by serpentine dehydration at sub-arc conditions from high pressure ophiolites in the Western Alps contains significant concentrations of B (2–30 µg/g) with a high $\delta^{11}B$ values (+9 to +28 ‰), whilst co-existing serpentine has 2–50 µg/g B with $\delta^{11}B$ = +6 to +24 ‰. Boron isotope fractionation between olivine and its precursor serpentine ($\Delta^{11}B_{ol-srp} = \delta^{11}B_{ol} - \delta^{11}B_{srp}$) is highly variable, which indicates significant isotopic disequilibrium between these minerals. Importantly, samples with B-enriched olivine have low $\Delta^{11}B_{ol-srp}$ (down to −9 ‰), evidence that olivine grew in the presence of a mixture of serpentine-derived fluids and external fluids with $\delta^{11}B$ of *ca.* +6 to +15 ‰. The composition of these external fluids is consistent with those from subducting sediments and altered oceanic crust at 50–80 km depth, and at least 15–45 % fluid addition. Our work shows that large scale slab fluid infiltration and fluid-mobile element transport accompanies serpentinite dehydration in subduction zones.

Introduction

The recycling of lithosphere-hosted volatile and fluid-mobile elements (*e.g.*, H_2O, CO_2, B, halogens) back into the convecting mantle *via* subduction has been crucial for Earth's evolution. Down-dragged mantle wedge serpentinites and hydrated oceanic mantle are water-rich (up to 13 wt. % H_2O), and increasingly recognised as important sources of water and fluid-mobile elements (Deschamps *et al.*, 2013; Scambelluri *et al.*, 2019). However, many details of serpentinite dehydration in subduction zones are still poorly understood, including the relative roles of mantle wedge *vs.* ocean floor serpentinites (Martin *et al.*, 2020) and B isotope fractionation during serpentine breakdown (De Hoog *et al.*, 2014). Previous work on B behaviour during de-serpentinisation in subduction settings focussed on whole rock geochemistry (Harvey *et al.*, 2014; Cannaò *et al.*, 2015), which obscures the detailed record of fluid-rock interaction preserved in individual mineral phases.

Metamorphic olivine is formed during breakdown of brucite or antigorite (high pressure serpentine) at ~400 °C and ~650 °C, respectively (Scambelluri *et al.*, 2004) and is B-rich (up to 100 µg/g; Scambelluri *et al.*, 2004; De Hoog *et al.*, 2014) compared to primary mantle olivine (<0.11 µg/g; Ottolini *et al.*, 2004). The incorporation of B in metamorphic olivine uniquely records fluid processes during serpentinite dehydration and allows insight into the composition, evolution and origin of these fluids.

Here we present *in situ* $\delta^{11}B$ data of co-existing serpentine and metamorphic olivine from high pressure serpentinites, which show significant disequilibrium between the two minerals. We interpret this as evidence for the infiltration of externally derived fluids during serpentinite dehydration, attesting to complex fluid pathways near the slab-wedge interface.

Samples and their Geological Setting

To capture the dehydration process, we selected eight serpentinite samples with phase assemblages between the brucite-out and antigorite-out phase transitions with 20–40 % modal olivine from three ophiolites in the Western Alps (Fig. 1). The Monviso Lago Superiore Unit (LSU) is a shear zone which underwent lawsonite-eclogite facies metamorphism and likely represents a serpentinite channel on the interface between the subducting plate and overlying mantle (Guillot *et al.*, 2004). The Zermatt-Saas ophiolite represents relict oceanic lithosphere of the Mesozoic Tethys ocean subducted to ~60–70 km: samples were obtained from near Zermatt and from Val d'Aosta. The Erro-Tobbio metaperidotites in the Voltri massif were subducted to 2.0–2.5 GPa and 550–600 °C and represent a subduction channel domain. See Supplementary Information for further sample details.

Boron Isotope Systematics of Olivine and Serpentine

Boron isotope ratios and concentrations were measured by SIMS at the Edinburgh Ion Microprobe Facility. Matrix-matched

1. School of GeoSciences, Grant Institute, The University of Edinburgh, James Hutton Road, EH9 3FE, United Kingdom
2. School of Earth and Environment, The University of Leeds, LS2 9JT, United Kingdom
3. Institut de Physique du Globe de Paris, Sorbonne Paris Cité, Université Paris Diderot, CNRS UMR 7154, Paris, France
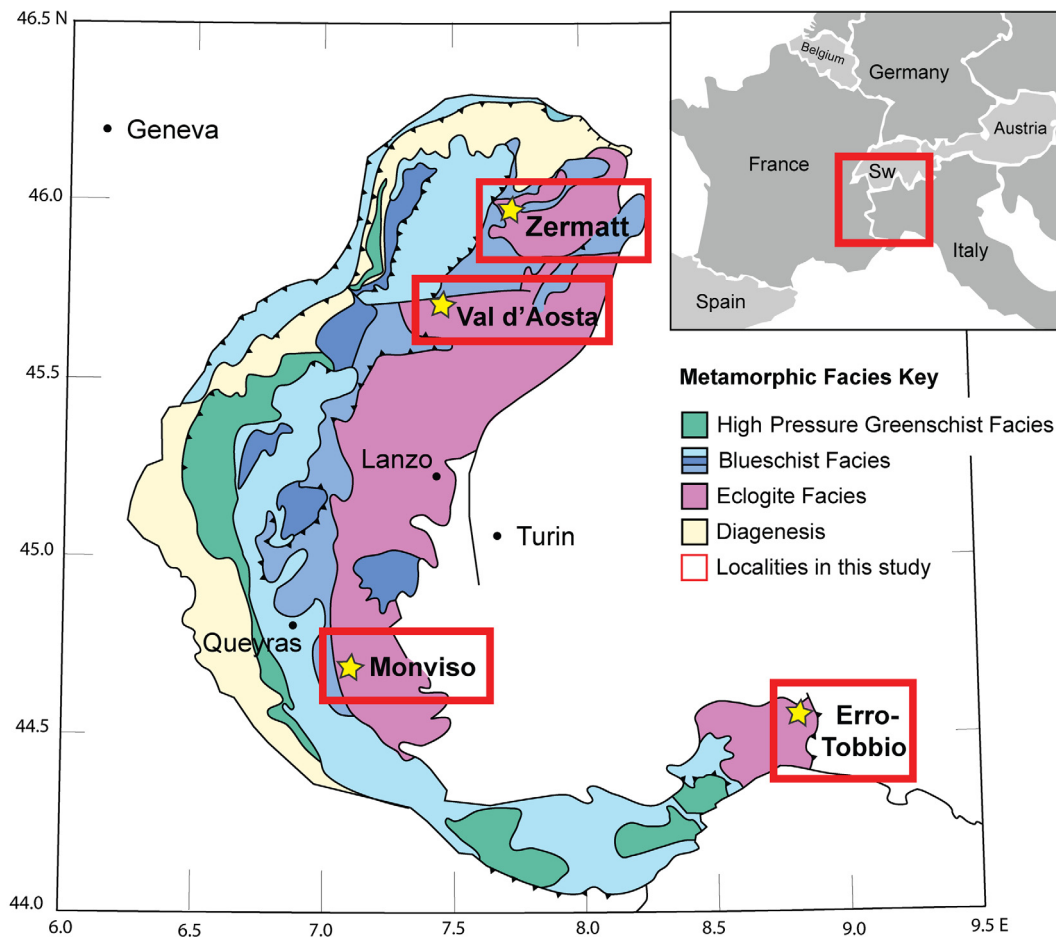* Corresponding author (email: ceesjan.dehoog@ed.ac.uk)

Figure 1 Metamorphic facies map of the Western Alps (after Bousquet *et al.*, 2012) showing study areas and sample locations.

standards including serpentine and olivine with known B isotope compositions were used for calibration. Typical uncertainty for B isotope analyses is ±1.6 ‰ (1s). Further analytical details and the complete dataset can be found in the Supplementary Information.

Olivine and serpentine show high $\delta^{11}B$ (+6 to +28 ‰) in all samples (Fig. 2). Minor phases present in some samples include pyroxene, chlorite and clinohumite. Clinohumite has similar [B] as olivine (4.8 to 6.5 µg/g), but very low modal abundance. Pyroxene and chlorite have low [B] (<2 µg/g) compared to olivine and serpentine and can be ignored for the overall B budget.

On average, Monviso metamorphic olivine shows lower $\delta^{11}B$ and higher [B] ($\delta^{11}B$ = +8 to +14 ‰, [B] ~16 µg/g) than co-existing serpentine ($\delta^{11}B$ = +18 to +21 ‰, [B] ~6 µg/g). Erro-Tobbio olivine has slightly higher $\delta^{11}B$ and [B] ($\delta^{11}B$ +18 to +20 ‰, [B] ~11 µg/g) than co-existing serpentine ($\delta^{11}B$ +16 to +17 ‰, [B] ~10 µg/g). Zermatt olivine shows a wide range of $\delta^{11}B$ (+16 to +28 ‰) and is higher on average than serpentine ($\delta^{11}B$ = +6 to +21 ‰), but lower [B] (~4 µg/g) in olivine compared to serpentine (~8 µg/g). The Val d'Aosta sample has higher [B] in olivine *vs.* serpentine (22 *vs.* 10 µg/g) but somewhat lower $\delta^{11}B$ (+17 to +19 ‰ in olivine, +16 to +21 ‰ in serpentine).

The most striking aspect of our dataset is the large variation in B isotope fractionation between olivine and serpentine ($\Delta^{11}B_{ol\text{-}srp}$; $\delta^{11}B_{ol}$ − $\delta^{11}B_{srp}$ of co-existing olivine and serpentine), which shows that olivine is often not in isotopic equilibrium with

serpentine, despite being its daughter product. Our dataset also shows a clear covariation between $\Delta^{11}B_{ol\text{-}srp}$ and B-enrichment in olivine ($[B]_{ol/srp}$: $[B]_{ol}/[B]_{srp}$): Zermatt metamorphic olivine is depleted in B compared to co-existing serpentine but has heavier $\delta^{11}B$ (Fig. 3). Monviso and Val d'Aosta olivine, however, is enriched in B compared to the co-existing serpentine but has lower $\delta^{11}B$. Erro-Tobbio olivine lies between these two extremes with roughly similar [B] and $\delta^{11}B$ in olivine and serpentine. As the measured olivine is metamorphic and grew upon serpentinite dehydration, protolith composition and heterogeneity have no bearing on $[B]_{ol/srp}$ and $\Delta^{11}B_{ol\text{-}srp}$, therefore processes operating during olivine growth are needed to explain these observations.

Fluid Infiltration during Serpentine Dehydration

No partitioning data for B between serpentine and olivine ($D_B^{ol/srp}$) is available, but a value of 3–5 for $D_B^{fluid/residue}$ was recorded during serpentinite dehydration experiments with olivine as the main reservoir for B in the residue (Tenthorey and Hermann, 2004). Given this, mass balance dictates that $D_B^{ol/srp} \sim 0.6$–0.9 (see Supplementary Information), and higher values indicate excess B in olivine. Samples from Zermatt show $[B]_{ol/srp}$ 0.4–0.9, close to the expected equilibrium value. This is accompanied by $\Delta^{11}B_{ol\text{-}srp}$ of +7.4 to +14.6 ‰ (Fig. 3). In most silicates, including serpentine, B^{3+} substitutes for Si^{4+} or Al^{3+} in tetrahedral (IV) coordination (Hervig *et al.*, 2002; Pabst *et al.*, 2011). In mantle
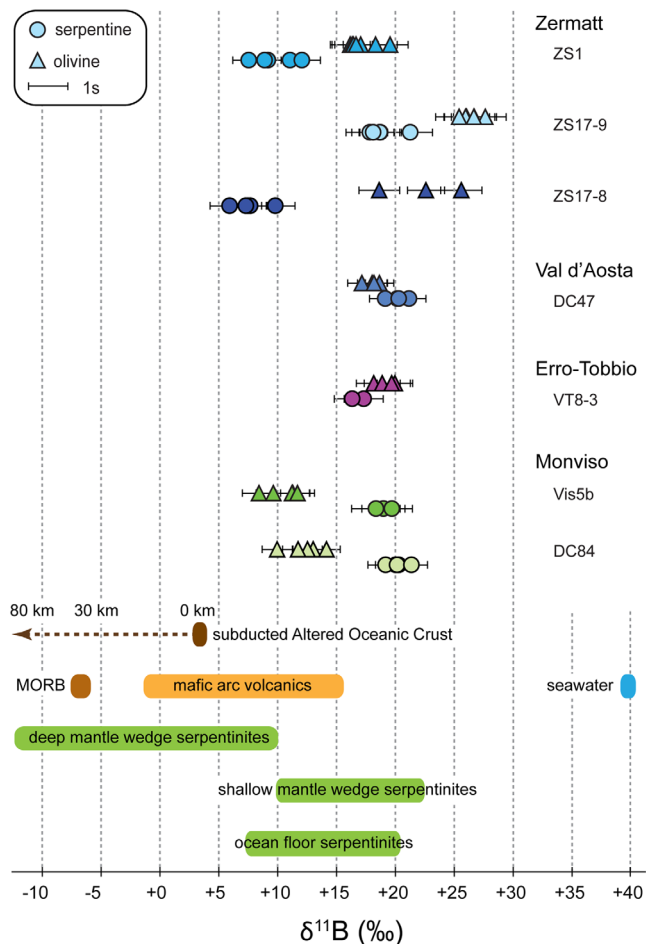
Figure 2 $\delta^{11}B$ data for olivine and serpentine in our samples. Error bars represent 1s uncertainties and include calibration uncertainties. Also indicated are B isotope compositions of various reservoirs relevant to subduction zones (data sources: Tonarini *et al.*, 2011; De Hoog and Savov, 2018 and references therein; Martin *et al.*, 2020).

Figure 3 Diagram comparing boron isotope systematics of co-existing metamorphic olivine and serpentine. $[B]_{ol/srp} = [B]_{olivine}/[B]_{serpentine}$, and $\Delta^{11}B_{ol-srp} = \delta^{11}B$ of olivine $-$ $\delta^{11}B$ of serpentine. Large symbols with 1s error bars indicate averages for each sample, whereas small symbols represent all possible olivine-serpentine pairs for each sample (see Supplementary Information for details). A broadly negative correlation between $[B]_{ol/srp}$ and $\Delta^{11}B_{ol-srp}$ is observed. Grey bars indicate equilibrium fractionation of boron and its isotopes at relevant *P-T* conditions.

silicates such as clinopyroxene and olivine, B also substitutes for Si^{4+} but occurs in trigonal (III) coordination as a BO_3 group (Hålenius *et al.*, 2010; Ingrin *et al.*, 2014). As ^{11}B preferentially resides in trigonal and ^{10}B in tetrahedral coordination (Kowalski *et al.*, 2013), olivine with trigonal B will show a heavier B isotope signature than co-existing serpentine with tetrahedral B. For the Zermatt samples, $\Delta^{11}B_{ol-srp}$ is close to the experimentally determined equilibrium B isotope fractionation between III and IV phases, which decreases from $\Delta^{11}B_{ol-srp} = +12.5$ to $+8.5$ ‰ with T increasing from 450 to 650 °C (Kowalski *et al.*, 2013).

Therefore, we conclude that Zermatt metamorphic olivine was in equilibrium with internal fluids released during dehydration of serpentine, with no evidence for contamination by external fluids. This conclusion is supported by REE and Sr isotope data (Gilio *et al.*, 2019) and consistent with the geological setting of the Zermatt samples, which come from a thick (~2 km) coherent section of subducted ocean lithosphere. The range in $\Delta^{11}B_{ol-srp}$ of $+7.4$ to $+14.6$ ‰ is probably related to metamorphic olivine forming at different temperatures during antigorite-out and brucite-out reactions, respectively.

The majority of metamorphic olivines from localities other than Zermatt have $[B]_{ol/srp} > 1$ and $\Delta^{11}B_{ol-srp} < +5$ ‰, *i.e.* more B and ^{10}B in olivine than is expected for growth during equilibrium dehydration of serpentine (Fig. 3). The most likely source of
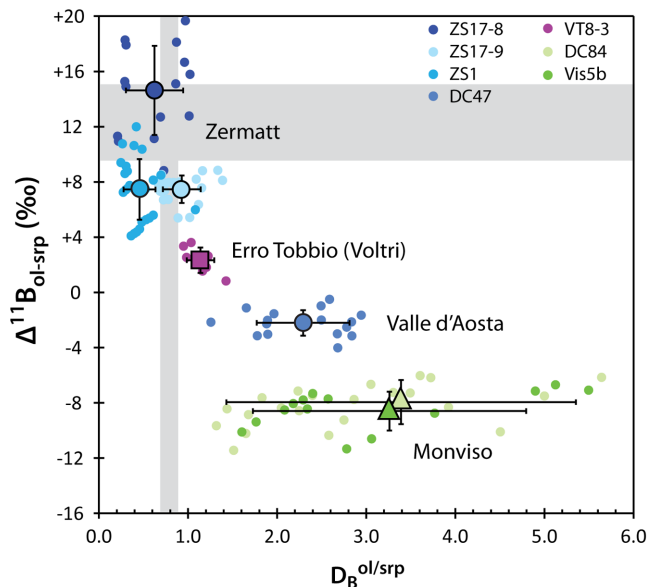
excess B is external fluid, as no other B-rich phases that dehydrate at 450–650 °C were present. Scarce clinohumite is B-rich but stable at the prevailing *P–T* conditions (Shen *et al.*, 2015) and its breakdown products (ilmenite, rutile) were not observed. Thus, we envisage a model where fluid from serpentine dehydration mixed with infiltrating external fluid, and metamorphic olivine grew in equilibrium with this mixed fluid. Serpentine did not re-equilibrate with this fluid due to sluggish kinetics at these low temperatures (450–650 °C) (*e.g.*, Lafay *et al.*, 2019). Mass balance calculations indicate that these external fluids had $\delta^{11}B$ of $+6$ ‰ (Monviso) to $+15$ ‰ (Erro-Tobbio) depending on the B concentration of the external fluids (Fig. S-6) and assuming mildly alkaline pH conditions for both internal and external fluids (Galvez *et al.*, 2016; Debret and Sverjensky, 2017). This matches the composition of fluids derived from a mixture of altered oceanic crust and sediments from 50–80 km depth (Tonarini *et al.*, 2011; Yamada *et al.*, 2019), consistent with the depth of the serpentinites in the former subduction zone. The external fluids comprise at least *ca.* 15–45 % of the total fluid budget of the dehydrating serpentinites, which are minimum estimates, as any partial re-equilibration of serpentine would lead to underestimating the amount of external fluid.

Metasomatism near the Subduction Interface

External fluids may permeate dehydrating serpentinites without the need for large scale faulting, as seen in Erro-Tobbio, which only shows metre scale vein networks and deformation. During serpentine dehydration there is a rapid increase in porosity and rock permeability allowing fluid to drain from the rock without the need for brittle failures and opening of fault pathways (Tenthorey and Cox, 2003; Plümper *et al.*, 2017). The creation of such porosity also provides pathways for significant volumes of B-rich external fluids to infiltrate.
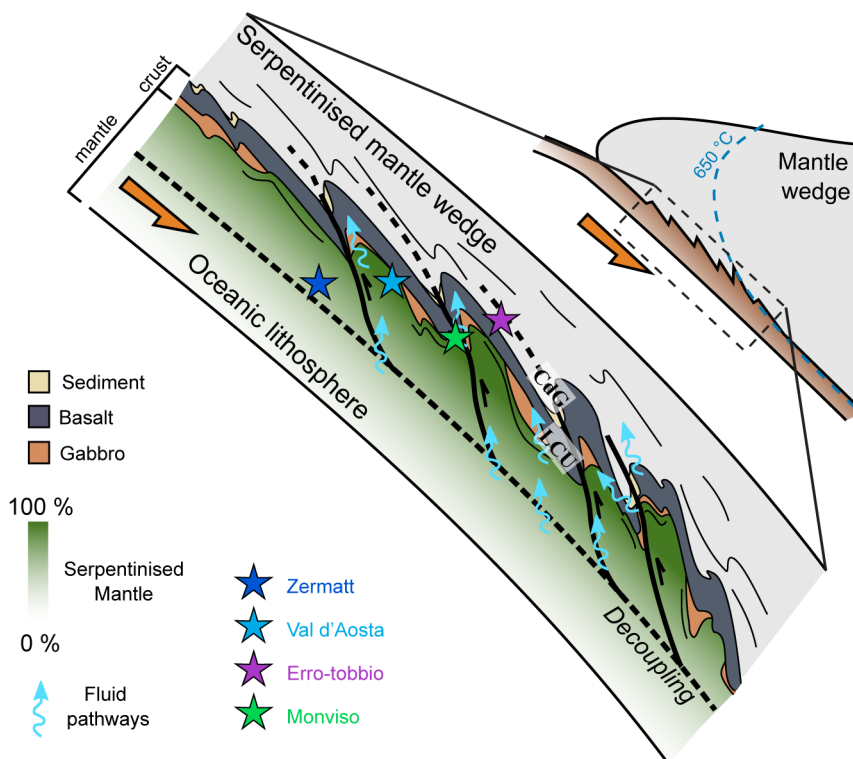
Figure 4 Schematic diagram depicting proposed fluid pathways and setting within the plate interface for serpentinite localities in this study after Gilio *et al.* (2019), where LCU and CdG indicate positions of Lago di Cignana and Cima di Gagnone HP ophiolites from that publication.

The trend towards higher $[B]_{ol/srp}$ with lower $\Delta^{11}B_{ol-srp}$ indicates an increasing influence of B-rich external fluids from Zermatt to Erro-Tobbio to Valle d'Aosta to Monviso. This trend correlates with the position of the serpentinite bodies relative to the slab-mantle interface during peak metamorphic conditions (Fig. 4). The Monviso ophiolite and Erro-Tobbio massif are thought to represent serpentinite domains between the subducting slab and the mantle wedge (Guillot *et al.*, 2004; Scambelluri and Tonarini, 2012); a prime location to be infiltrated by fluids derived from the subducted slab. Shear zone associated faulting provides many additional pathways for fluid flow throughout the Monviso ophiolite, leaving the serpentinites exposed to extensive interaction with external fluids (Angiboust *et al.*, 2014; Gilio *et al.*, 2020). The Val d'Aosta sample is considered part of the Zermatt-Saas ophiolite but at Val d'Aosta the serpentinite is thinner (~0.5 km) and surrounded by crustal lithologies (metasediments and metabasalts). This sample shows elevated $[B]_{ol/srp}$ and lower $\Delta^{11}B_{ol-srp}$ compared to the other Zermatt samples, likely related to its proximity to other lithologies and increased exposure to dehydration fluids.

The micro-scale process where metamorphic olivine grows from a mixture of internal and external fluids would not be detected using whole rock $\delta^{11}B$ data, as serpentinites in this study have positive whole rock $\delta^{11}B$ (*e.g.*, Scambelluri and Tonarini, 2012) whilst being variably affected by external fluid infiltration. In contrast, subduction mélange serpentinites and metaperidotites with negative $\delta^{11}B$ suffered more extensive contamination and extreme $\delta^{11}B$ overprinting consistent with their close association with large proportions of crustal rocks and sediments (Cannaò *et al.*, 2015; Martin *et al.*, 2020).

Conclusions

Metamorphic olivine is a sensitive recorder of the fluid composition from which it grew, and recorded extensive external fluid infiltration during subduction dehydration of Alpine serpentinites,

which are sinks and carriers of crust-derived fluid mobile elements. External fluid infiltration was most prominent in serpentinites close to the subduction interface and amounted to up to 45 % of the total dehydration fluid budget. The study of B isotope systematics of texturally co-existing olivine and serpentine provides a powerful tool to study fluid flow deep in subduction zones, and reveals processes not visible in whole rock $\delta^{11}B$ compositions.

Acknowledgements

Additional Information

Supplementary Information accompanies this letter at https://www.geochemicalperspectivesletters.org/article2039.

author. Additional information is available at https://www.geochemicalperspectivesletters.org/copyright-and-permissions.

Cite this letter as: Clarke, E., De Hoog, J.C.M, Kirstein, L.A., Harvey, J., Debret, B. (2020) Metamorphic olivine records external fluid infiltration during serpentinite dehydration. *Geochem. Persp. Let.* 16, 25–29.

References

Angiboust, S., Pettke, T., De Hoog, J.C.M., Caron, B., Oncken, O. (2014) Channelized fluid flow and eclogite-facies metasomatism along the subduction shear zone. *Journal of Petrology* 55, 883–916.

Bousquet, R., Oberhänsli, R., Schmid, S.M., Berger, A., Wiedenkehr, C.R., Möller, A., Rosenberg, C., Zeilinger, G., Molli, G., Koller, F. (2012) Metamorphic framework of the Alps. CCGM-CGMW, Paris.

Cannaò, E., Agostini, S., Scambelluri, M., Tonarini, S., Godard, M. (2015) B, Sr and Pb isotope geochemistry of high-pressure Alpine metaperidotites monitors fluid-mediated element recycling during serpentinite dehydration in subduction mélange (Cima di Gagnone, Swiss Central Alps). *Geochimica et Cosmochimica Acta* 163, 80–100.

De Hoog, J.C.M., Savov, I.P. (2018) Boron Isotopes as a Tracer of Subduction Zone Processes. In: Marschall, H., Foster, G. (Eds.) *Boron Isotopes: The Fifth Element. Advances in Isotope Geochemistry.* Springer International Publishing, Cham, 217–247.

De Hoog, J.C.M., Hattori, K., Jung, H. (2014) Titanium- and water-rich metamorphic olivine in high-pressure serpentinites from the Voltri Massif (Ligurian Alps, Italy): evidence for deep subduction of high-field strength and fluid-mobile elements. *Contributions to Mineralogy and Petrology* 167.

Debret, B., Sverjensky, D.A. (2017) Highly oxidising fluids generated during serpentinite breakdown in subduction zones. *Scientific Reports* 7, 10351.

Deschamps, F., Godard, M., Guillot, S., Hattori, K. (2013) Geochemistry of subduction zone serpentinites: A review. *Lithos* 178, 96–127.

Galvez, M.E., Connolly, J.A.D., Manning, C.E. (2016) Implications for metal and volatile cycles from the pH of subduction zone fluids. *Nature* 539, 420–424.

Gilio, M., Scambelluri, M., Agostini, S., Godard, M., Peters, D., Pettke, T. (2019) Petrology and geochemistry of serpentinites associated with the ultra-high pressure Lago di Cignana Unit (Italian Western Alps). *Journal of Petrology* 60, 1229–1262.

Gilio, M., Scambelluri, M., Agostini, S., Godard, M., Pettke, T., Agard, P., Locatelli, M., Angiboust, S. (2020) Fingerprinting and relocating tectonic slices along the plate interface: Evidence from the Lago Superiore unit at Monviso (Western Alps). *Lithos* 352, 105308

Guillot, S., Schwartz, S., Hattori, K., Auzende, A.L., Lardeaux, J. (2004) The Monviso ophiolitic massif (Western Alps), a section through a serpentinite subduction channel. *Journal of the Virtual Explorer* 16, 1–17.

Hålenius, U., Skogby, H., Eden, M., Nazzareni, S., Kristiansson, P., Resmark, J. (2010) Coordination of boron in nominally boron-free rock forming silicates: Evidence for incorporation of BO_3 groups in clinopyroxene. *Geochimica et Cosmochimica Acta* 74, 5672–5679.

Harvey, J., Garrido, C.J., Savov, I., Agostini, S., Padrón-Navarta, J.A., Marchesi, C., Sánchez-Vizcaíno, V.L., Gómez-Pugnaire, M.T. (2014) [11]B-rich fluids in subduction zones: The role of antigorite dehydration in subducting slabs and boron isotope heterogeneity in the mantle. *Chemical Geology* 376, 20–30.

Hervig, R.L., Moore, G.M., Williams, L.B., Peacock, S.M., Holloway, J.R., Roggensack, K. (2002) Isotopic and elemental partitioning of boron between hydrous fluid and silicate melt. *American Mineralogist* 87, 769–774.

Ingrin, J., Kovacs, I., Deloule, E., Balan, E., Blanchard, M., Kohn, S.C., Hermann, J. (2014) Identification of hydrogen defects linked to boron substitution in synthetic forsterite and natural olivine. *American Mineralogist* 99, 2138–2141.

Kowalski, P.M., Wunder, B., Jahn, S. (2013) Ab initio prediction of equilibrium boron isotope fractionation between minerals and aqueous fluids at high P and T. *Geochimica et Cosmochimica Acta* 101, 285–301.

Lafay, R., Baumgartner, L.P., Putlitz, B., Siron, G. (2019) Oxygen isotope disequilibrium during serpentinite dehydration. *Terra Nova* 31, 94–101.

Martin, C., Flores, K.E., Vitale-Brovarone, A., Angiboust, S., Harlow, G.E. (2020) Deep mantle serpentinization in subduction zones: Insight from in situ B isotopes in slab and mantle wedge serpentinites. *Chemical Geology* 545, 119637.

Ottolini, L., Le Fèvre, B., Vannucci, R. (2004) Direct assessment of mantle boron and lithium contents and distribution by SIMS analyses of peridotite minerals. *Earth and Planetary Science Letters* 228, 19–36.

Pabst, S., Zack, T., Savov, I.P., Ludwig, T., Rost, D., Vicenzi, E.P. (2011) Evidence for boron incorporation into the serpentine crystal structure. *American Mineralogist* 96, 1112–1119.

Plümper, O., John, T., Podladchikov, Y.Y., Vrijmoed, J.C., Scambelluri, M. (2017) Fluid escape from subduction zones controlled by channel-forming reactive porosity. *Nature Geoscience* 10, 150–156.

Scambelluri, M., Tonarini, S. (2012) Boron isotope evidence for shallow fluid transfer across subduction zones by serpentinized mantle. *Geology* 40, 907–910.

Scambelluri, M., Müntener, O., Ottolini, L., Pettke, T.T., Vannucci, R. (2004) The fate of B, Cl and Li in the subducted oceanic mantle and in the antigorite breakdown fluids. *Earth and Planetary Science Letters* 222, 217–234.

Scambelluri, M., Cannaò, E., Gilio, M. (2019) The water and fluid-mobile element cycles during serpentinite subduction. A review. *European Journal of Mineralogy* 31, 405–428.

Shen, T.T., Hermann, J., Zhang, L.F., Lu, Z., Padrón-Navarta, J.A., Xia, B., Bader, T. (2015) UHP metamorphism documented in Ti-chondrodite- and Ti-clinohumite-bearing serpentinized ultramafic rocks from Chinese Southwestern Tianshan. *Journal of Petrology* 56, 1425–1457.

Tenthorey, E., Cox, S.F. (2003) Reaction-enhanced permeability during serpentinite dehydration. *Geology* 31, 921–924.

Tenthorey, E., Hermann, J. (2004) Composition of fluids during serpentinite breakdown in subduction zones: Evidence for limited boron mobility. *Geology* 32, 865–868.

Tonarini, S., Leeman, W.P., Leat, P.T. (2011) Subduction erosion of forearc mantle wedge implicated in the genesis of the South Sandwich Island (SSI) arc: Evidence from boron isotope systematics. *Earth and Planetary Science Letters* 301, 275–284.

Yamada, C., Tsujimori, T., Chang, Q., Kimura, J.I. (2019) Boron isotope variations of Franciscan serpentinites, northern California. *Lithos* 334, 180–189.

Metamorphic olivine records external fluid infiltration during serpentinite dehydration

E. Clarke, J.C.M. De Hoog, L.A. Kirstein, J. Harvey, B. Debret

Supplementary Information

The Supplementary Information includes:

- ➢ 1. Analytical Methods
- ➢ 2. Geological Context of Samples
- ➢ 3. Sample Descriptions
- ➢ 4. Background Geochemical Data
- ➢ 5. Average $[B]_{ol/srp}$ and $\Delta^{11}B_{ol\text{-}srp}$ Calculations
- ➢ 6. Estimate of Equilibrium $D_B{}^{ol/srp}$
- ➢ 7. Modelling of External Fluid Composition
- ➢ Supplementary Tables
- ➢ Supplementary Information References

1. Analytical Methods

Major element analyses

Major element analyses were conducted by EPMA using the Cameca SX-100 at the University of Edinburgh using thin sections prepared from the hand specimens. Sections were carbon coated before analysis. Analytical set up (counting times, beam current, spot size) was tailored to each phase individually, here is a summary. Spot size varied from 2 to 8 µm depending on phase (defocussed spot for hydrous phases), accelerating voltage was set at 15 kV. Beam current varied from 2 to 100 nA depending on phase and element, with higher current used for minor elements, which were analysed subsequently to the major elements. Peak counting times varied from 20 to 120 s and background counting times varied from 10 to 100 s. Data were calibrated using certified mineral standards.

Fluid Mobile Element concentration analyses

B, Li, F, Cl and H_2O data were obtained by SIMS using the Cameca IMS-4f ion microprobe at the NERC IMF at the University of Edinburgh. Thin sections were cut into 25 mm rounds and gold coated before analysis. For all phases, a 5 nA primary beam of $^{16}O^-$ ions accelerated to 14.5 kV was

used to impact the sample. The spot size was ~15 µm and pit depth <2 µm. Prior to the start of each analysis the analytical area was cleaned using a 120 s pre-sputter with a 25 µm raster. Secondary ions were filtered based on their energy (75 ±20 eV) and counted using a single electron multiplier. Total counting times per analysis (divided into six mass cycles) were 18 s for ^{1}H, 30 s for ^{7}Li, ^{11}B, 12 s for ^{26}Mg, ^{27}Al and ^{30}Si, and 60 s for ^{19}F and ^{35}Cl. Analyses were calibrated using basaltic glass standards St81-A9 (Lesne *et al.*, 2011), GSD1-G and BCR-2G (preferred values in GeoReM; Jochum *et al.*, 2005, except B in GSD is 65 µg/g, Walowski *et al.*, 2019), using ^{30}Si as an internal standard with SiO_2 from EPMA data.

In situ B isotope analyses

Boron isotope ratios were measured by SIMS using the Cameca IMS-1270 ion microprobe at the NERC IMF at the University of Edinburgh. A primary beam of $^{16}O_2^-$ ions was accelerated to 22.5 kV with a beam current of 25–30 nA (pyroxene, olivine, chlorite, serpentine). Analysis time, including pre-sputtering, was around 26 minutes per spot and resulted in a spot size of ~20 µm. Each analysis was divided into 100 cycles with counting times of 8 s for ^{10}B and 2 s for ^{11}B, respectively. To calculate the isotope ratio for each analysis, each ^{11}B value was divided by the average of ^{10}B measured directly before and after, resulting in 99 ratios in total (as no ^{10}B value was measured after the last ^{11}B value). Internal precision was calculated as the standard error, i.e., standard deviation of 99 ratios divided by the square root of 99.

Drift was monitored and data was calibrated using the glass standards BCR-2G, GOR128-G and StHs6/80-G (Jochum *et al.*, 2000) for olivine and serpentine standards (srp-21826; SY347; Geiss1) for serpentine, as previous work suggested significant matrix effects for hydrous minerals (De Hoog *et al.*, 2017). The use of the glass calibration for olivine was later confirmed as accurate by analysis of a newly acquired olivine mineral standard Koh (δ^{11}B = -4.6 ±0.8 ‰, measured as bulk powder by MC-ICP-MS after fusion digestion in Pisa by Eleri Clarke and Samuele Agostini, and after HF digestion in Bristol by Andre Paul), which showed no offset within analytical uncertainty. Matrix effects have previously been shown to be insignificant for B isotope measurements by SIMS for anhydrous silicate glasses other than NIST SRM610-616, in a study including komatiites and rhyolites (Marschall and Monteleone, 2015). This is in sharp contrast with matrix effects observed for Li isotopes, in which even the Fo content of olivine has an effect (Bell *et al.*, 2009). Although we do not have multiple olivine B isotope standards with different Fo contents, the lack of matrix effects in the anhydrous silicate glasses and the fact that our single olivine standard falls on the silicate glass trend indicates that our data (Fo_{87}–Fo_{96}) was not affected by matrix effects.

In contrast, analysis of three serpentine standards, measured in bulk independently by TIMS, revealed an offset of on average -6.6 ±0.9 ‰ compared to glass standards (**Fig. S-1**). The serpentine standards have somewhat lower Mg# (**Table S-1**) than our samples (**Table S-5**), but no matrix effect (correlation of Mg# with δ^{11}B offset) was apparent.

Calibration of B isotope measurements was done by calculating the slope of measured ^{11}B/^{10}B ratios *vs.* reference ^{11}B/^{10}B ratios for the calibration standards (ranging from 0.953–0.974 for glasses and 0.947–0.967 for serpentines) and using these values to correct measured ^{11}B/^{10}B ratios of the samples. The uncertainties of the calibration slopes (ca. 0.9 ‰) were propagated into the analytical uncertainties presented in **Table S-3**. Boron isotope ratios are presented as delta values (in ‰) relative to standard (SRM951 ^{11}B/^{10}B ratio of 4.04362 (Catanzaro *et al.*, 1970) using the equation: $\delta^{11}B_{sample} = 1000[(R_{sample}/R_{SRM951}) - 1]$ where R = ^{11}B/^{10}B ratio.

Table S-1 Major element composition by EPMA of mineral standards for B isotope analysis.

Sample	SiO_2	Al_2O_3	Cr_2O_3	FeO	MnO	NiO	MgO	CaO	Na_2O	Total	Mg#
Koh-ol	40.1	n.a.	<0.04	5.5	0.10	0.43	53.9	<0.01	<0.02	100.03	94.6
SRP-21826	42.23	2.87	0.34	6.43	0.11	0.26	36.10	0.02	<0.02	88.37	90.9
SRP-SY347	42.20	2.50	0.34	7.73	0.10	0.24	34.83	0.03	<0.02	87.98	88.9
SRP-GEISS1	43.55	2.40	0.15	5.00	0.10	0.20	36.30	0.11	<0.02	87.80	92.8
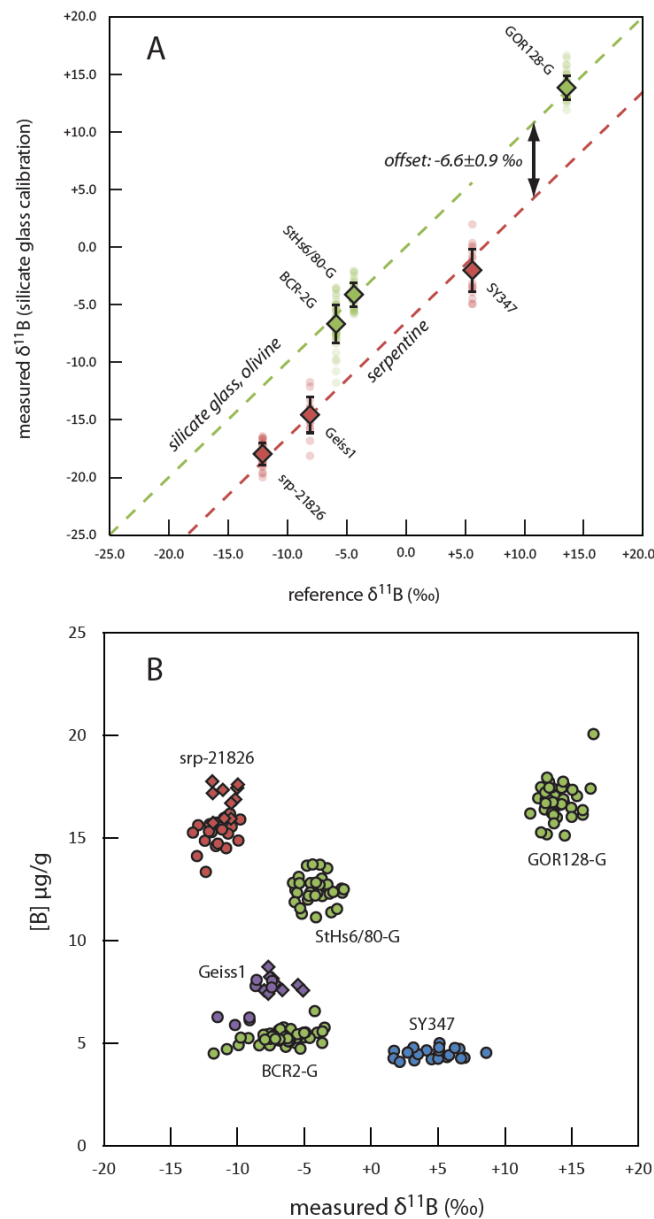
Figure S-1 (a) Measured $\delta^{11}B$ calibrated using silicate glasses *vs*. reference $\delta^{11}B$. Note the offset for the serpentine standards of -6.6 ‰. Individual analytical points as well as average ±1s are indicated. (b) Measured $\delta^{11}B$ (calibrated using serpentine standards for serpentine and glass standards for silicate glasses) *vs*. measured B concentration. Glasses indicated with green symbols, serpentine in other colours. If multiple grains were measured for serpentines these are indicated with different symbols (two grains each for srp-21826 and Geiss1). BCR2-G data is from four different fragments on several different mounts. Data for srp-21826 was previously published in Pabst *et al*. (2012).

2. Geological Context of Samples

Monviso

The Monviso Lago Superiore Unit (LSU) is a shear zone comprising metabasalts, metagabbros and serpentinites, which underlies the Monviso Unit and overlies the Dora Maira metasediments. The Monviso ophiolite was subducted to a depth of ~80 km (Groppo and Castelli, 2010), reaching lawsonite-eclogite facies metamorphism about 45 Ma (Rubatto and Herman, 2003) with a maximum *P–T* of 550 °C at 2.6 GPa (Angiboust *et al.* 2012). The ophiolite is widely considered to represent ancient Tethyan ocean floor (*e.g.* Rubatto and Angiboust, 2015). Guillot *et al.* (2004) proposed that the Monviso ophiolite represents a serpentinite channel on the interface between the subducting plate and overlying mantle. The presence of the shear zone provides many pathways for fluid flow throughout the ophiolite (Angiboust *et al.*, 2014; Gilio *et al.*, 2020) leaving the serpentinites exposed to extensive interaction with external fluids. Samples Vis5B and DC84 preserve metamorphic olivine veins amongst patches of antigorite and rare relict pyroxene. The former was collected from serpentinites in the lower shear zone of the LSU and has been discussed previously by Debret *et al.* (2013). The latter was collected from the LSU basal serpentinites nearby, where samples show evidence of infiltration by crustal fluids (Gilio *et al.*, 2020).

Zermatt and Val d'Aosta (Zermatt-Saas ophiolite)

The Zermatt-Saas ophiolite comprises antigorite schists, metagabbros, metabasalts and sheeted dyke complexes, and is thought to represent relict oceanic lithosphere of the Mesozoic Tethys ocean of harzburgitic composition (*e.g.* Li *et al.*, 2004; Angiboust *et al.*, 2009; Gilio *et al.*, 2019). Metamorphism occurred during subduction to ~60–70 km depth followed by exhumation during the Alpine orogeny (Barnicoat and Fry, 1986) between 34 to 14 Ma (Amato *et al.*, 1999), with maximum *P–T* conditions of 600 °C at 2.5 GPa (Rebay *et al.*, 2012). At this locality, however, there is little to no evidence of external fluids, indicating that the serpentinites have remained relatively isolated from other lithologies during their metamorphic history (Gilio *et al.*, 2019). Many 'ZS' samples contain metamorphic olivine veins in antigorite matrix that are in some places associated with clinohumite, chlorite, pyroxene or magnetite. Metamorphic olivine is in all cases associated with antigorite shards. Samples were collected from a ~2 km thick serpentinite unit in the Zermatt-Saas Ophiolite (primarily from just east of Trockener Steg near the town of Zermatt).

Sample DC47 was also collected from the Zermatt-Saas ophiolite but from a distal location (Servette, Valle d'Aosta). Here serpentinite is more closely associated (few 100 m) with hydrothermally altered meta-sediments and metabasalts. The sediments overlying the metabasalts are interpreted to be the cover sequence of the oceanic lithosphere (Tartarotti *et al.*, 1986). Peak conditions reached in this locality were 2.1 GPa and 550 °C (Martin *et al.*, 2008).

Erro-Tobbio (Voltri Massif)

The Erro-Tobbio metaperidotite is a lherzolitic unit at a high stratigraphic level within the Voltri Massif, which comprises meta-sediments, metagabbros and serpentinites (Capponi and Crispini, 2002). It underwent serpentinisation and was subducted to 2.0–2.5 GPa and 550–600 °C during the Cretaceous (145–66 Ma) (Scambelluri *et al.*, 1991; Scambelluri *et al.*, 1995). The serpentinites of Erro-Tobbio are suggested to be former oceanic mantle hydrated (serpentinised) in a mantle wedge domain (Scambelluri and Tonarini, 2012). Lower stratigraphic parts of the Voltri Massif were serpentinised on the seafloor and endured further fluid-rock interactions within subduction channel domains (Cannaò *et al.*, 2016), but are distinct from the Erro-Tobbio unit. Erro-Tobbio serpentinites have a strong foliation defined by antigorite and chlorite, with parallel veins of metamorphic olivine

and clinohumite. Sample VT8-3 (as in de Hoog *et al*., 2014) was collected from one of these veins. Also contains relic pyroxene and chlorite.

3. Sample Descriptions

Table S-2   Brief descriptions of samples in this study. **Figure S-2** shows examples of serpentinite textures found in these samples. Mineral abbreviations as in Kretz (1983). Erro-Tobbio sample (VT8-3) from De Hoog *et al*. (2014), Monviso sample (Vis5b) from Debret *et al*. (2013).

Locality	Sample nr.	Mineral assemblage	Textures
Zermatt 45° 58' 04''N 07° 44' 04''E	ZS17-8	srp + chu + ol + mag + di	Ol and chu form veins around atg patches with px cores. Shards of atg are found included in ol or on grain boundaries
Zermatt 45° 58' 06''N 07° 43' 58''E	ZS17-9	srp + ol + mag + chl	Thick (2mm) veins of ol2 in atg matrix with minor chlorite
Zermatt In vicinity of ZS17-8,9	ZS1	ol + srp + mag	Foliated with two distinct types: interlocking ol and atg. Ol included by atg shards
Valle d'Aosta 45° 42' 11''N 07° 27' 19''E	DC47	srp + ol + mag	Elongate patches of ol in atg matrix
Monviso 44° 41' 52''N 07° 05' 35''E	DC84	srp + ol + px + mag	Veins of atg + ol around relict px
Monviso In vicinity of DC84	Vis5b	srp + ol + mag	Ol in veins amongst patches of atg
Erro-Tobio (Voltti Massif) 44° 33.677' N 08° 48.907' E	VT8-3	srp + chl + ol + chu + px +mag	Foliation forming atg + chl with veins of ol + chu. Ol contain low-Ti mag

Metamorphic olivine

Metamorphic olivine can be distinguished from primary (relict) olivine both texturally and chemically. Metamorphic olivines tend to have higher Mg# (88.7 to 96.5) due to Fe sequestration in magnetite during serpentinisation, higher MnO (0.2 to 0.5 wt %, **Table S-4**), and higher [B] most likely due to their formation by brucite and/or antigorite breakdown than typical primary mantle olivine (Fo90–92, MnO <0.2 wt.%, De Hoog *et al*., 2010). Metamorphic olivine often has antigorite inclusions. Texturally, metamorphic olivine in this study forms veins or elongate clusters (see **Fig. S-2**) and such veins are often associated with dehydration reactions (Healy *et al*., 2009; López Sánchez-Vizcaíno *et al*., 2009), whereas relict primary olivines are often preserved in the cores of serpentine mesh textures (*e.g.* Rouméjon and Cannat, 2014). No primary olivine was preserved in any of our samples.

Serpentine (antigorite)

Serpentine was abundant in all samples and was essentially identified as antigorite by crystal shape (short laths) and high Al_2O_3 (1.3–2.1 wt%) contents, but this was not confirmed by Raman spectrometry. However, it is in agreement with the high-pressure origin of these rocks and consistent with literature about serpentinites from the localities studied here (*e.g.*, Scambelluri *et al.*, 1995; Debret *et al.*, 2013; Angiboust *et al.*, 2014; Kempf and Hermann, 2018). Serpentine in late-stage veins had low Al_2O_3 and may be lizardite, but this was again not confirmed by Raman spectrometry.
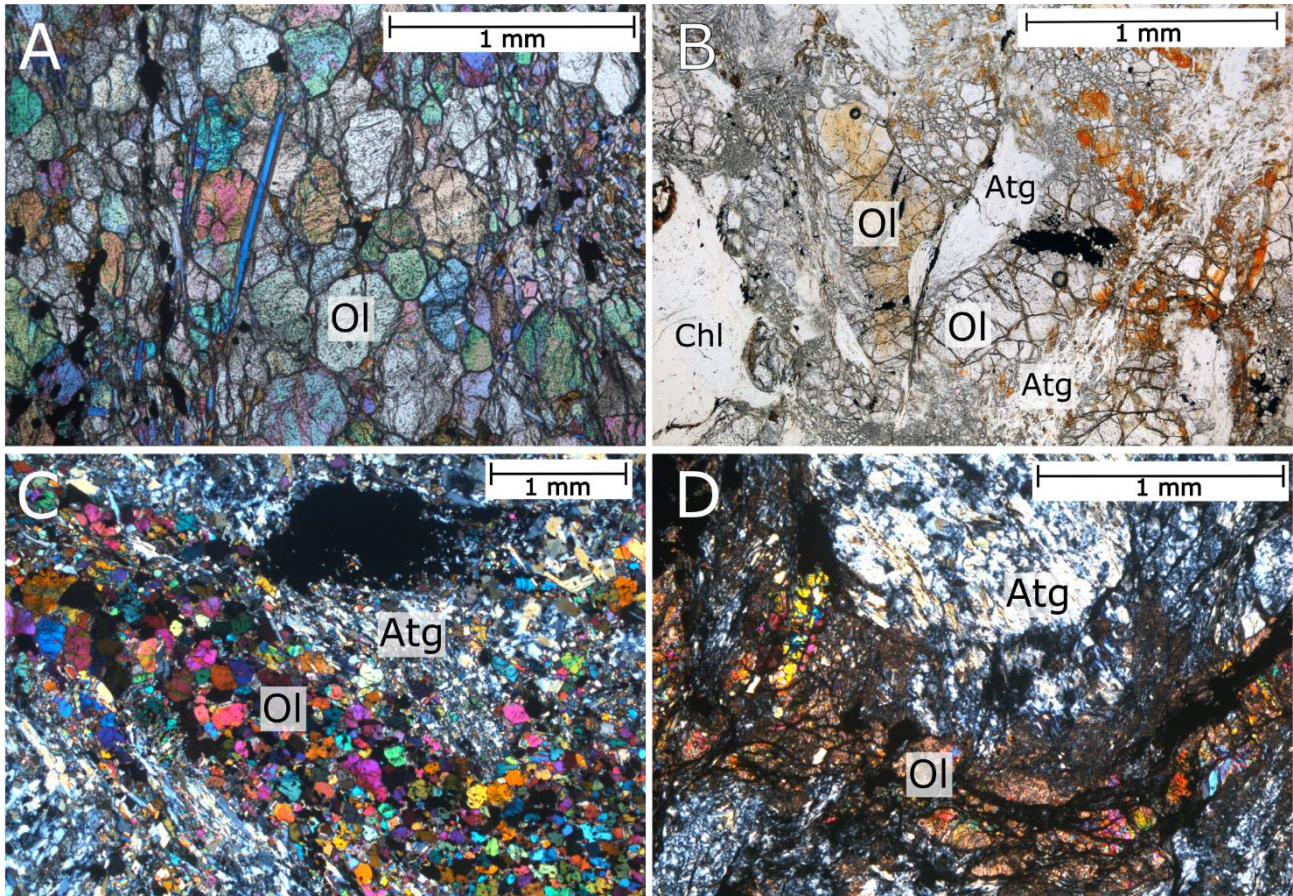
Figure S-2 Textures of metamorphic olivine in thin sections. **(a)** Zermatt: Thin section XP images of metamorphic olivine veins in a matrix of antigorite. **(b)** Erro-Tobbio: Thin section PPL image of secondary olivine, antigorite and chlorite in Erro-Tobbio sample VT8-3 from De Hoog *et al.* (2014). Small dark orange grains are clinohumite. **(c)** Zermatt: Thin section XP images of metamorphic olivine veins in a matrix of antigorite. **(d)** Monviso: Thin section XP image of metamorphic olivine vein in matrix of antigorite.

4. Background Geochemical Data

Major elements

Major element data for the olivine, serpentine and other silicates are presented in **Table S-4, S-5** and **S-6**, respectively. Samples from the **Zermatt-Saas ophiolite** make up the majority of the samples in this study. They contain Fo_{94-97} olivine (except Val d'Aosta sample DC47: Fo_{92}) with MnO ~ 0.2–0.4 wt % and NiO ~0.21–0.27 wt %. Antigorite has Mg# ~96–97 and Al_2O_3 ~1.2–2.1 wt %. Pyroxene is scarce and diopsidic, with a Mg# ~98 and CaO ~26.0 wt%. Clinohumite is Ti-rich TiO_2 ~3.3–4.1 wt%, Mg# ~96, MnO ~0.3 wt% and NiO ~0.2 wt%.

Sample VT8-3 from **Erro-Tobio (Voltri Massif)** was described by De Hoog *et al*. (2014); olivine has lower Fo contents (~Fo_{87}) than Zermatt olivine but similar MnO ~0.3 wt % and NiO ~0.3 wt %. Some high TiO_2 up to 0.9 wt % values are present due to the presence of clinohumite defects, but these do not correlate with B contents. Clinohumite is Ti-rich (4.7–7.8 wt %) and has lower Mg# (~86) then Zermatt clinohumite with similar MnO ~0.4 wt% and NiO ~0.2 wt%. Antigorite is similar to that from Zermatt with high Mg# (~95) and ~2.6 wt % Al_2O_3. Clinopyroxene is Ca-rich (22.9–25.6 wt %) and have variable Al_2O_3 (0.1–5.5 wt %), where the Al-poor cpx is remnant primary cpx and Al-poor cpx represents late stage metamorphic overgrowth.

Samples from the **Monviso ophiolite** (Vis5B (Debret *et al*., 2013) and DC84) contain lower Fo olivine (Fo_{87-92}) than the rest of the samples but contain similar MnO ~ 0.3–0.4 wt % and NiO ~0.05–0.46 wt %. Monviso antigorite has high Mg# ~96 and Al_2O_3 ~1.5–2.3 wt %.

Fluid-mobile elements

Boron contents are variable (~1 to ~30 µg/g in serpentine and secondary olivine). Secondary olivine also contains high concentrations of other FMEs (F: ~5–50 µg/g, Cl: ~0–40 µg/g and Li: ~0.1–11.5 µg/g) (see **Table S-3**) and contains more Li than co-existing serpentine. Minor serpentinite phases: chlorite, clinohumite, pyroxene and amphibole also contain appreciable amounts of FMEs, including B (up to 11.9 µg/g). We briefly summarise the FME data below, but we provide this data for completeness and discussion is beyond the scope of this study. FME contents of antigorite are inherited from the protolith or the serpentinising fluids, but have little bearing on the serpentine dehydration process studied here.

Monviso secondary olivine shows higher Li (~0.11–0.19 µg/g) and B (~12–17 µg/g) compared to serpentine (Li ~ 0.01–0.02 µg/g and B 4 – 5 µg/g). F and Cl concentrations are more similar between secondary olivine (F ~19 µg/g and Cl ~20 µg/g) and serpentine (F ~15 µg/g and Cl ~19 µg/g). Pyroxene has very low B (0.5 µg/g), moderate F (10 µg/g) and Cl (13 µg/g), and higher Li (1.3 µg/g) than secondary olivine.

Zermatt (incl. **Val d'Aosta**) secondary olivine shows higher Li (~0.1–1.7 µg/g) and B (~2–20 µg/g) overall compared to serpentine (Li ~ 0.01–0.03 µg/g and B ~ 3.0–11 µg/g), but lower F (~8–12 µg/g) and Cl (~3–11 µg/g) concentrations compared to serpentine (F ~18–21 µg/g and Cl ~6–31 µg/g). Other phases are rich in FMEs: Chlorite (where present) has lower B (~1.6 µg/g) but similar Li (~0.06 µg/g), F (~17 µg/g) and Cl (~33 µg/g) to serpentine. Clinohumite shows similar Li (~0.3–0.4 µg/g), B (~5–12 µg/g) and Cl (~6–10 µg/g) to secondary olivine but much higher concentrations of F (~112–658 µg/g). Diopside contains similar Li (~0.6 µg/g), F (~8 µg/g) and Cl (~7 µg/g) to olivine but less B (~2.5 µg/g).

Erro-Tobbio (Voltri) data is from De Hoog *et al*. (2014). Secondary olivine contains high B (9–23 µg/g) and very high Li (4–47 µg/g) compared to olivine from other localities in this study.

5. Average $[B]_{ol/srp}$ and $\Delta^{11}B_{ol\text{-}srp}$ Calculations

Due to difficulty in finding serpentine of sufficient size and adequate polish for analysis it was often not possible to measure adjacent serpentine and olivine grains. Therefore, $[B]_{ol/srp}$ and $\Delta^{11}B_{ol\text{-}srp}$ could not be calculated based on measurements of discrete mineral pairs. Averaging all B isotope and concentration data for each mineral phase may introduce bias if any heterogeneity is present in the samples. To determine the length scale of any potential sample heterogeneities we plotted $\Delta^{11}B_{ol\text{-}srp}$ for all possible serpentine-olivine pairs in each sample against the distance between the analytical spots (**Fig. S-3**). For example, if 3 olivines and 4 serpentines were measured in a sample, twelve $\Delta^{11}B_{ol\text{-}srp}$ values and distances were calculated. In addition, we plotted $\Delta^{11}B$ for all possible olivine-olivine and serpentine-serpentine pairs.

Most samples showed no correlation between $\Delta^{11}B_{ol\text{-}srp}$ values and distance, indicating that these were homogeneous at the scale of (the measured area of) the thin section (**Fig. S-3**). However, for sample ZS17-9 any pairs that were more than 8 mm apart show an offset of 2–4 ‰ in $\Delta^{11}B_{ol\text{-}ol}$ and $\Delta^{11}B_{srp\text{-}srp}$ as well as increased scatter for $\Delta^{11}B_{ol\text{-}srp}$. A plot of X-Y positions of the analytical points labelled with $\delta^{11}B$ values shows a small but significant difference between the left and right side of the sample for olivine as well as serpentine (**Fig. S-4**). Importantly, $\Delta^{11}B_{ol\text{-}srp}$ in the two domains is similar, as otherwise a larger scatter on the plot of distance *vs* $\Delta^{11}B_{ol\text{-}srp}$ would be observed for distances <8 mm. Therefore, we conclude that the two different domains are related to the original sample heterogeneity of the protolith (serpentinite), which was inherited by later metamorphic olivine. Likewise, small $\delta^{11}B$ heterogeneities of on a scale of ca. 4 mm can be seen in sample ZS-1, but again the effect on $\Delta^{11}B_{ol\text{-}srp}$ is limited. As taking average $\delta^{11}Bol$ – average $\delta^{11}Bsrp$ may lead to bias if there are an unequal number of analyses of serpentine and olivine from heterogeneous domains, the average $\Delta^{11}B_{ol\text{-}srp}$ for each sample was calculated averaging $\Delta^{11}B_{ol\text{-}srp}$ values of all possible olivine-serpentine pairs in the sample. The uncertainty in the average $\Delta^{11}B_{ol\text{-}srp}$ is calculated as the standard deviation in the average of all possible pairs. This data is presented in Fig. 3 in the main text.
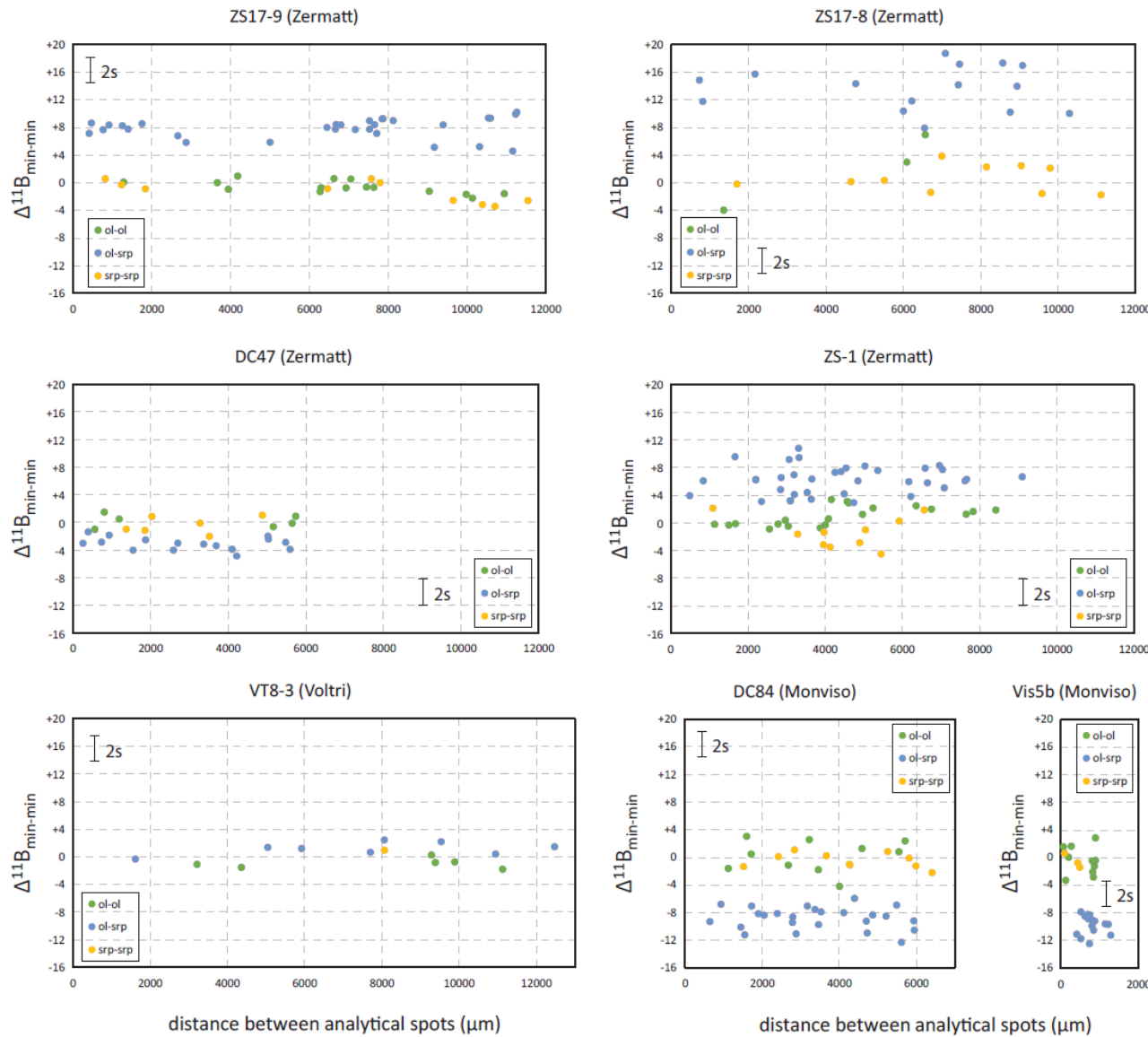
Figure S-3 Boron isotope fractionation between mineral pairs *vs.* their distance from each other. For each analytical spot, the difference between all other analytical spots from the same sample are indicated and colour coded by mineral. For example, if a sample has three olivine grains and two serpentine grains analysed, three olivine-olivine pairs are indicated (ol1-ol2, ol1-ol3 and ol2-ol3), one serpentine pair (srp1-srp2) and six olivine-serpentine pairs (ol1-srp1, ol1-srp2, ol2-srp1, ol2-srp2, ol3-srp1, ol3-srp2). Note that $\Delta^{11}B$ for ol-ol and srp-srp pairs are close to zero and show little correlation with distance, showing homogeneous boron isotopic compositions. Only sample ZS-1 shows increased fractionation for spots >4000 µm apart, and ZS17-9 for spots >9000 µm apart due to different domains having slightly different olivine and serpentine $\delta^{11}B$ values. In contrast, large differences in boron isotope fractionation are observed for ol-srp pairs in different samples. These fractionation differences show little correlation with distance between the points, again indicating consistent behaviour on thin-section scale.
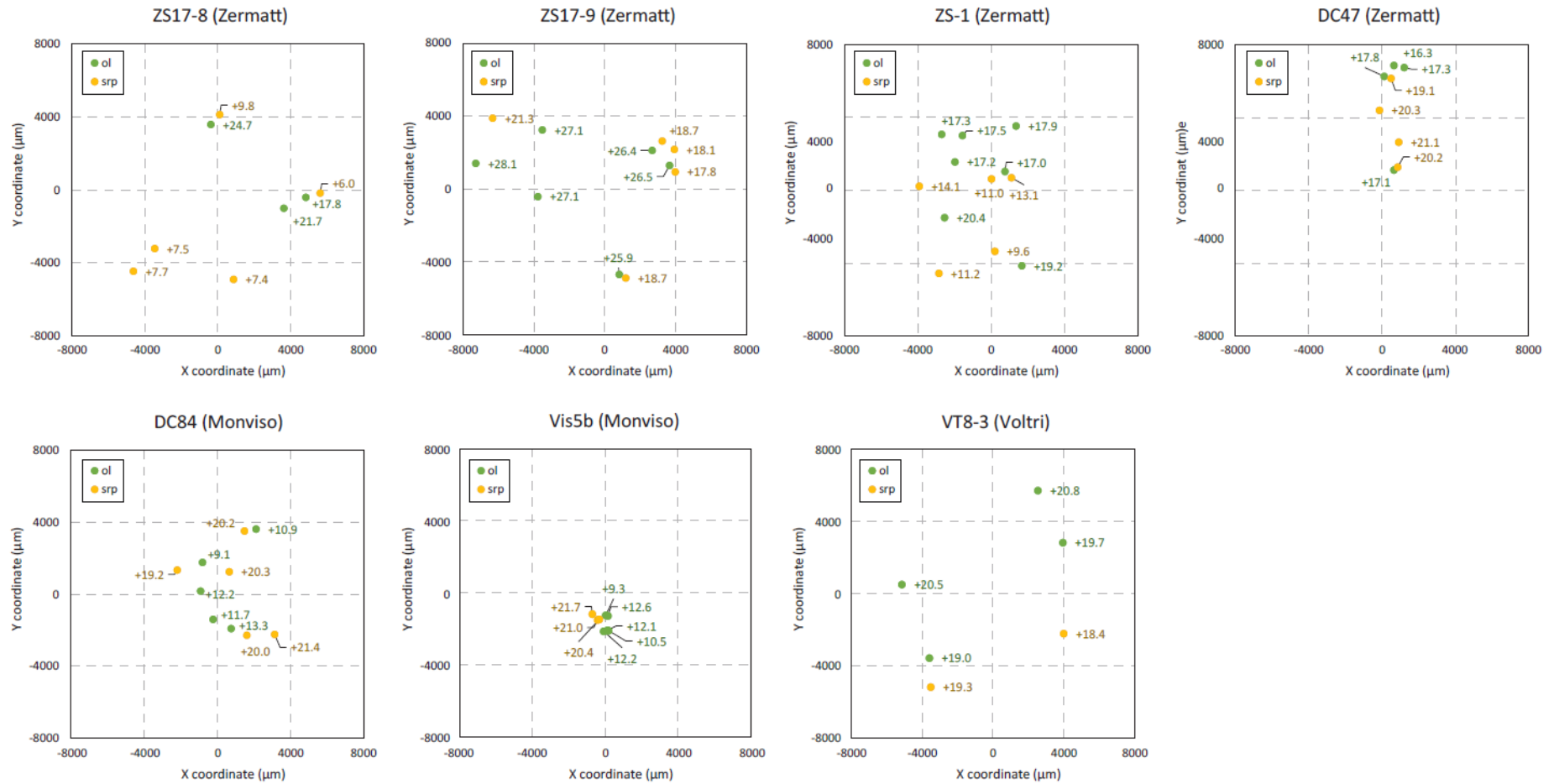
Figure S-4   X-Y coordinates of all analytical spots colour-coded by mineral (olivine and serpentine) to show their spatial relationship. δ^{11}B values are indicated for each spot.

6. Estimate of Equilibrium $D_B^{ol/srp}$

No literature $D_B^{ol/srp}$ value is available, so it was calculated based on dehydration experiments by Tenthorey and Hermann (2004). First, we needed to estimate $D_B^{fl/ol}$. A value of $D^{fl/residue}$ of 3–5 was presented by Tenthorey and Hermann (2004) for their serpentinite dehydration experiments. Olivine was shown to be the major host for B in the residue, but about 10 % modal orthopyroxene and chlorite were present in the experiments, which is consistent with serpentine having a higher Si/Mg ratio than olivine. Both orthopyroxene and chlorite have lower affinity for B than olivine ($D_B^{ol/chl}$ = 3–4 and $D_B^{ol/opx}$ = 1.3–3; Tenthorey and Hermann, 2004), and can therefore be ignored in the overall B budget, but their presence does slightly modify the estimate for $D_B^{fl/ol}$. Mass balance calculations result in a value of $D_B^{fl/ol}$ = 2.8–4.7.

$D_B^{fl/ol}$ values were also presented by Scambelluri *et al*. (2004) based on fluid inclusion data, which average to about 5 and broadly agree with the values of Tenthorey and Hermann (2004). However, these values were considerably more scattered and dependent on assumptions about salinity of the fluid (Scambelluri *et al*., 2004). Therefore, we regard the Tenthorey and Hermann (2004) the more reliable estimate of $D_B^{ol/srp}$.

$D_B^{ol/srp}$ can be derived using the following equation:
$$D_B^{ol/srp} = \frac{1}{D^{fl/ol} \times Fr_{fl} + Fr_{ol}}$$

with $D^{fl/ol}$ = 2.8–4.7, Fr_{fl} = 0.13 and Fr_{fl} = 0.84, where Fr is the fraction of either olivine or fluid produced by the breakdown of serpentine. This gives a value of 0.68–0.81 for $D_B^{ol/srp}$. We model this based on serpentine containing 13 wt.% H_2O, and a residue containing 87 wt.% olivine. However, serpentine has higher Si/Mg than olivine and therefore either some Opx must form or excess Si is transported away in the fluid. The effect of this on the above calculations is only small: incorporating 10 wt% Opx in the residue with $D_B^{ol/opx}$ = 3 would result in $D_B^{ol/srp}$ values of 0.70–0.85 instead. To take into account these uncertainties we have used a range of $D_B^{ol/srp}$ 0.68–0.85 for equilibrium partitioning in our modelling.

7. Modelling of External Fluid Composition

The B isotopic composition of external fluids infiltrating during serpentinite dehydration can be estimated based on compositions of co-existing olivine and serpentine. For this model we assume the following dehydration environment: as serpentine breaks down it releases a B-bearing aqueous internal fluid and creates new metamorphic olivine. When externally derived fluids infiltrate the pore spaces, these mix with the serpentine-breakdown fluid, and metamorphic olivine grows in isotopic equilibrium with the mixed fluid (**Fig. S-5**). Serpentine does not re-equilibrate with the mixed fluid, as evidenced by the large range of $\Delta^{11}B_{ol\text{-}srp}$ in our samples, which is incompatible with olivine and serpentine both being in equilibrium with the mixed fluid. Slow diffusion of B in serpentine at the conditions of serpentinite dehydration (450–650 °C) are probably the cause of this lack of re-equilibration. Our model simulates this mixing process and calculates the composition of the externally derived fluid.
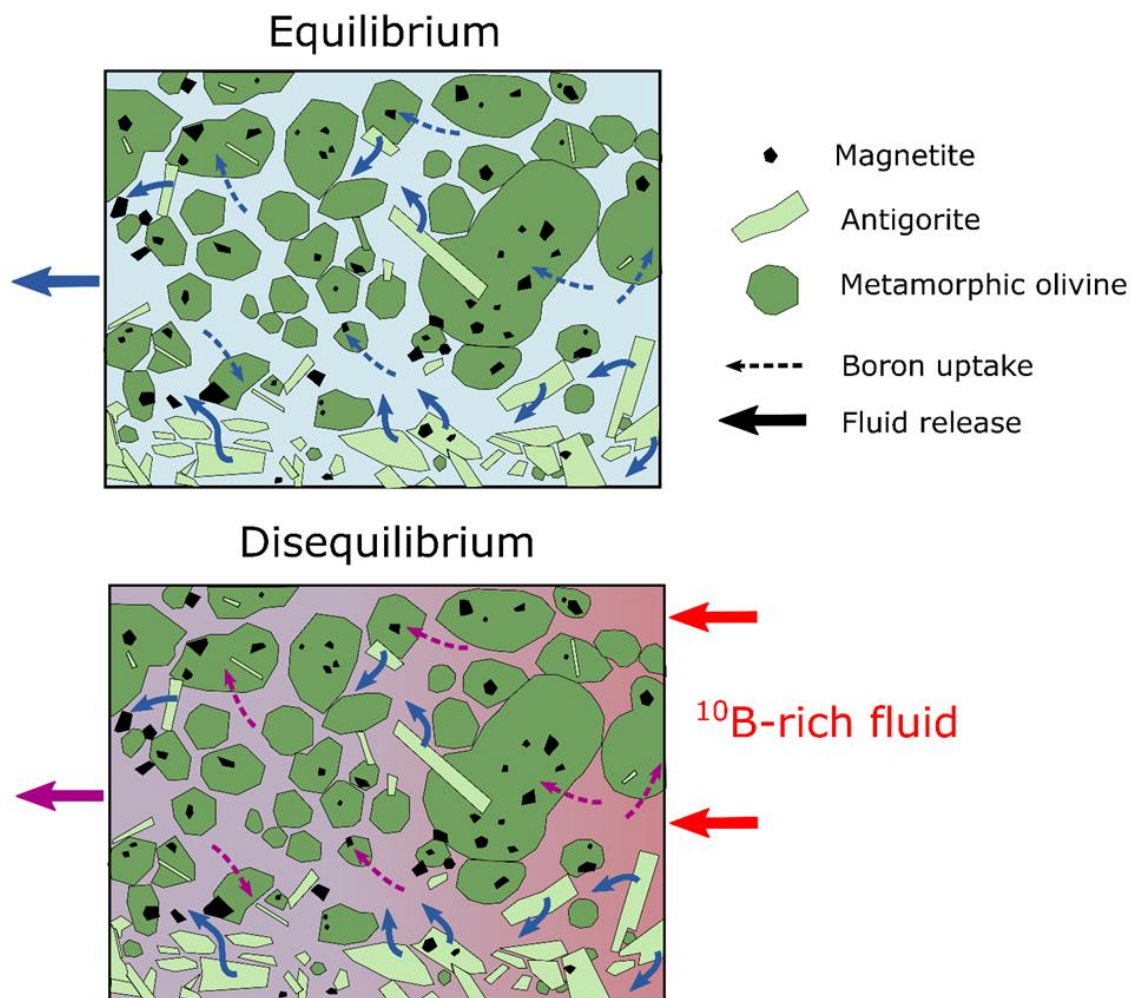
Figure S-5   Schematic diagram depicting two different scenarios of serpentine dehydration. **(a)** Breakdown of serpentine releases fluid and creates metamorphic olivine. The volume change of the solid components creates porosity (*e.g.* Tenthorey and Cox, 2003). As all fluid is produced internally, olivine and serpentine will be in B isotopic equilibrium. **(b)** If B-bearing external fluids infiltrate during serpentine dehydration and mix with the serpentine breakdown fluids, metamorphic olivine will not be in isotope equilibrium with serpentine. Serpentine compositions are unlikely to be affected by the external fluid, as exchange of B between serpentine and fluid is limited by slow diffusion at the low temperatures involved.

We calculate the range of possible external fluid compositions based on the compositions of the serpentine fluid and the mixed fluid using the following equations:

Internal (serpentine dehydration) fluid

$$[B]_{\text{int-fl}} = D_B^{\text{fl/srp}} \times [B]_{\text{srp}}$$

$$\delta^{11}B_{\text{int-fl}} = \delta^{11}B_{\text{srp}} + \Delta^{11}B_{\text{srp-fl}}$$

where $\Delta^{11}B_{\text{srp-fl}} = 0$ ‰ at 650 °C as there will be little to no fractionation between IV sites in silicates and IV sites in mildly alkaline fluids (Williams *et al*., 2001), and $D_B^{\text{fl/srp}} = D^B_{\text{fl/ol}} \times D^B_{\text{ol/srp}} = 2.3$–$3.3$. B_{srp} and $\delta^{11}B_{\text{srp}}$ are the average measured serpentine compositions in a sample. pH of the internal fluid during serpentinite dehydration is about 5, whereas neutral pH at these conditions is about 3.5 (Debret and Sverjensky, 2017), thus $B(OH)_4$ is the main B species in the fluid.

Mixed fluid (in equilibrium with olivine)

$$[B]_{\text{mix-fl}} = D_B^{\text{fl/ol}} \times [B]_{\text{ol}}$$

$$\delta^{11}B_{\text{mix-fl}} = \delta^{11}B_{\text{ol}} + \Delta^{11}B_{\text{ol-fl}}$$

where $\Delta^{11}B_{\text{ol-fl}} = -9.8$ ‰ at 650°C based on the isotopic fractionation of B between III-coordinated B in olivine and IV-coordinated B in mildly alkaline fluids (Williams *et al*., 2001), and $D^B_{\text{fl/ol}} = 2.8$–4.7. B_{ol} and $\delta^{11}B_{\text{ol}}$ are the average measured olivine compositions in a sample.

If the internal fluid is the same as the mixed fluid, the system is in equilibrium and no external fluid is needed to explain the olivine and serpentine compositions. If an external fluid were present, it would have the same composition as the internal fluid, and cannot be detected.

External fluid

The mixed fluid is a mixture of internal and external fluid, so the composition of the latter can be calculated by mass balance if the compositions of mixed and internal fluid are known. However, since the B concentration of the fluid is not known, we can only calculate the $\delta^{11}B$ of the external fluid ($\delta^{11}B_{\text{ext-fl}}$) as a function of assumed B content ($[B]_{\text{ext-fl}}$). These are the curves presented in **Fig. S-6**. We assume that B speciation in the external fluid is similar to that of the internal fluid (*i.e.*, dominated by $B(OH)_4$), as crustal-derived fluids at subduction-zone conditions are mildly alkaline, similar to serpentinite-derived fluids (Galvez *et al*., 2016; Debret and Sverjensky, 2017).

For the mass balance calculation we mix ^{10}B and ^{11}B individually, which results in the B concentration ($[B] = [^{10}B] + [^{11}B]$) as well as the B isotope ratio $^{11}B/^{10}B$, from which $\delta^{11}B$ can be derived:

$$[^{10}B]_{\text{mix-fl}} = [^{10}B]_{\text{int-fl}} \cdot Fr + [^{10}B]_{\text{ext-fl}} \cdot (1\text{-}Fr)$$

$$[^{11}B]_{\text{mix-fl}} = [^{11}B]_{\text{int-fl}} \cdot Fr + [^{11}B]_{\text{ext-fl}} \cdot (1\text{-}Fr)$$

where Fr = fraction of internal fluid added, and ^{10}B and ^{11}B were calculated from $\delta^{11}B$ and $[B]$ of the mixed fluid and internal fluid as follows:

$$[^{10}B]_{fl} = \frac{[B]_{fl}}{SRM \times \left(\frac{\delta^{11}B_{fl}}{1000} + 1\right) + 1} \quad \text{and} \quad [^{11}B]_{fl} = [B]_{fl} - [^{10}B]_{fl}, \text{ where } SRM = {}^{11}B/{}^{10}B \text{ of SRM951 (4·04362;}$$

Catanzaro *et al.*, 1970), for which $\delta^{11}B$ is zero by definition.

Uncertainties in input parameters ($D_B^{fl/srp}$, $[B]_{srp}$, $\delta^{11}B_{srp}$, $D_B^{fl/ol}$, $[B]_{ol}$, $\delta^{11}B_{ol}$ where taken into account, which is why the mixing curves are shown as fields and not as lines in **Fig. S-6**.
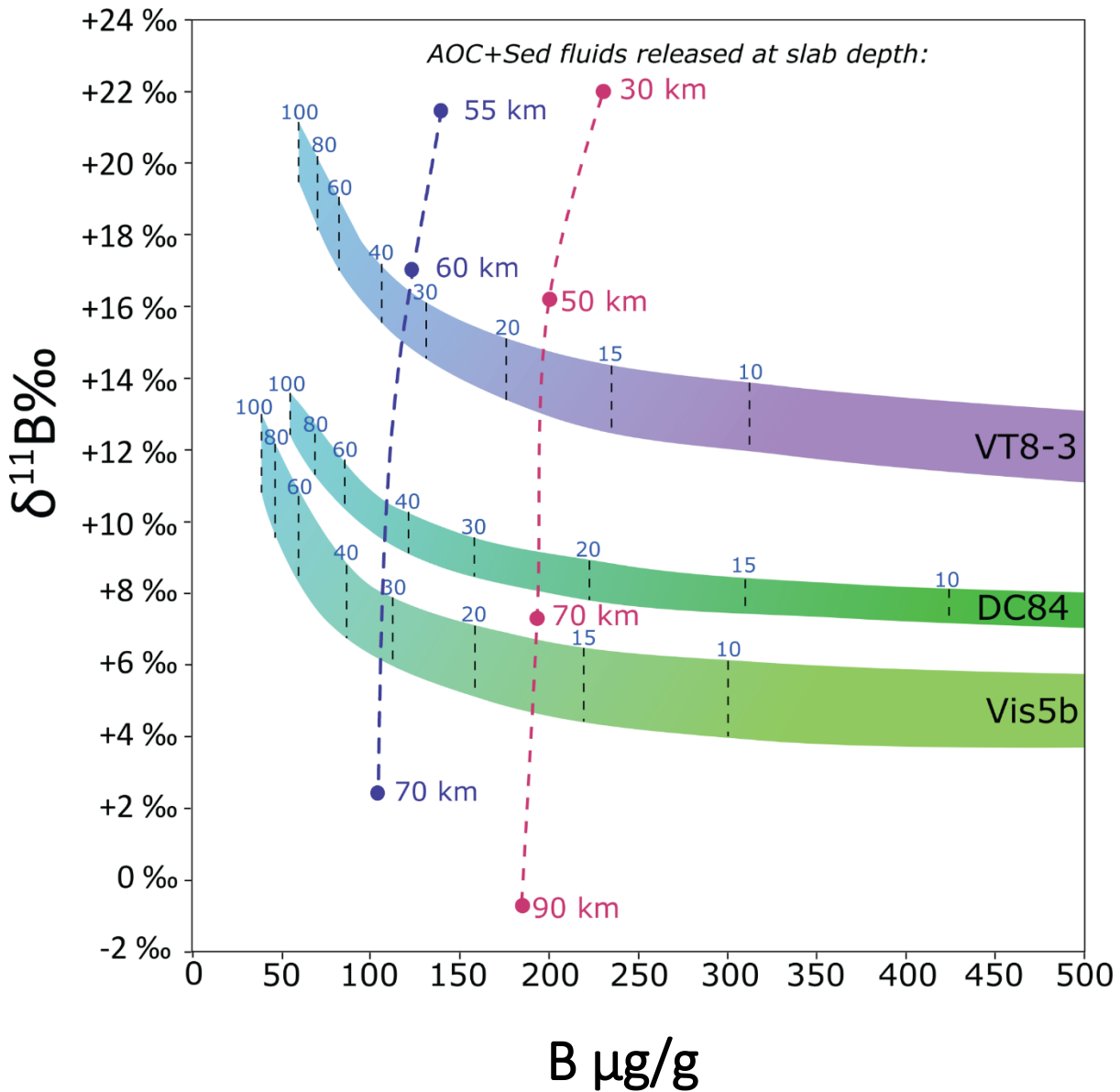
Figure S-6   Plot of $\delta^{11}B$ *vs.* B concentration showing the possible range of compositions of external fluid needed to produce the olivine compositions in different localities. Blue numbers indicate the percentage of external fluid mixing with serpentine fluid, where 50 % is a 1:1 mixture. External fluids are predicted to have exclusively positive $\delta^{11}B$. Also indicated are model compositions of slab-derived fluids at various depths of the slab (red line: 90 % AOC + 10% sediment; Tonarini *et al.*, 2011; blue line: 70 % AOC + 30 % sediment; Yamada *et al.*, 2019).

Table S-3   Boron isotopic compositions FME concentrations (µg/g) of olivine (OL) and serpentine (SRP).

Phase	Analysis code (B isotope spot)	X pos	Y pos	$\delta^{11}B$ ‰	1s ‰	B µg/g (1270)	B µg/g (4f)	Li µg/g	F µg/g	Cl µg/g	H_2O wt. %
Zermatt (ZS17-8)											
OL	66_ZS17-8-OL	-383	3574	+ 25.5	±1.8	3.6	4.9	1.7	11.0	4.2	<d.l
OL	61_ZS17-8-OL	4840	-408	+ 18.6	±1.7	2.6	n.a.	n.a.	n.a.	n.a.	n.a.
OL	62_ZS17-8-OL	3626	-1012	+ 22.5	±1.6	3.6	n.a.	n.a.	n.a.	n.a.	n.a.
SRP	65_ZS17-8-SRP	108	4116	+ 9.8	±1.7	3.6	3.6	<d.l	13.2	7.6	14.3
SRP	63_ZS17-8-SRP	5627	-180	+ 6.0	±1.7	3.8	5.3	<d.l	26.4	7.8	13.6
SRP	72_ZS17-8-SRP	-3463	-3212	+ 7.5	±1.7	4.2	10.1	<d.l	18.0	5.8	13.9
SRP	71_ZS17-8-SRP	-4625	-4456	+ 7.7	±1.4	12.1	n.a.	n.a.	n.a.	n.a.	n.a.
SRP	73_ZS17-8-SRP	866	-4904	+ 7.3	±1.3	12.6	n.a.	n.a.	n.a.	n.a.	n.a.
Zermatt (ZS17-9)											
OL	84_ZS17-9-OL	3675	1296	+ 26.0	±1.9	1.4	1.8	1.2	7.6	0.8	<d.l
OL	86_ZS17-9-OL	2683	2120	+ 25.9	±1.8	1.7	2.3	0.6	9.6	2.4	<d.l
OL	93_ZS17-9-OL	831	-4688	+ 25.4	±2.0	1.4	1.9	1.2	5.1	2.2	<d.l
OL	92_ZS17-9-OL	-3770	-418	+ 26.6	±1.7	1.7	1.9	1.5	8.3	0.7	<d.l
OL	91_ZS17-9-OL	-7274	1404	+ 27.6	±1.8	1.8	3.2	0.4	7.7	6.9	0.1
OL	89_ZS17-9-OL	-3518	3242	+ 26.6	±1.9	1.4	1.7	0.8	8.9	3.8	<d.l
SRP	83_ZS17-9-ATG	3984	940	+ 17.9	±2.0	1.2	2.7	<d.l	19.3	5.9	13.9
SRP	87_ZS17-9-ATG	3255	2632	+ 18.7	±1.8	2.0	1.7	<d.l	16.0	3.8	13.5
SRP	94_ZS17-9-ATG	1192	-4890	+ 18.7	±1.7	1.8	5.6	<d.l	16.9	8.4	13.6
SRP	85_ZS17-9-ATG	3936	2174	+ 18.1	±1.8	2.1	3.3	<d.l	10.8	9.3	14.2
SRP	90_ZS17-9-ATG	-6317	3888	+ 21.3	±1.9	1.6	1.6	<d.l	27.1	2.5	14.7
Zermatt (ZS1)											
OL	11_ZS-ol11 S	-2545	-1497	+ 19.5	±1.5	7.4	8.5	0.5	7.7	8.8	<d.l
OL	12_ZS-ol12 S	1670	-4125	+ 18.3	±1.8	4.6	8.7	1.0	5.9	5.7	<d.l
OL	7_ZS-ol7 L	751	1035	+ 16.1	±1.7	5.1	7.9	0.4	6.1	1.8	<d.l
OL	8_ZS-ol8 S	-1978	1557	+ 16.3	±1.7	5.7	5.9	0.6	8.8	1.8	<d.l
OL	15_ZS-ol15 L	1360	3520	+ 17.0	±1.5	11.6	n.a.	n.a.	n.a.	n.a.	n.a.
OL	3_ZS-ol3 S	-2701	3070	+ 16.4	±1.6	6.0	n.a.	n.a.	n.a.	n.a.	n.a.
OL	4_ZS-ol4 S	-1566	3005	+ 16.6	±1.8	6.5	n.a.	n.a.	n.a.	n.a.	n.a.
SRP	13_ZS-atg13	203	-3340	+ 7.6	±1.3	17.9	21	<d.l	119.0	78.9	14.1
SRP	6_ZS-atg6	1105	690	+ 11.1	±1.6	10.8	22.4	<d.l	126.0	90.0	14.0
SRP	14_ZS-atg14	-2852	-4549	+ 9.2	±1.4	15.5	50.5	<d.l	598.0	84.4	14.5
SRP	5_ZS-atg5	17	623	+ 8.9	±1.4	19.1	13.8	<d.l	104.0	85.7	13.1
SRP	9_ZS-atg9	-3917	229	+ 12.1	±1.6	14.4	12.8	<d.l	124.0	39.2	13.4

<d.l. = less than detection limit, for H_2O <0.02 and otherwise <0.1. n.a = not analysed. 1270 refers to isotope analysis, 4f to trace element analysis. X pos and Y pos are sample stage coordinates in µm.

Table S-3   Continued

Phase	Analysis code (B isotope spot)	X pos	Y pos	$\delta^{11}B$ ‰	1s ‰	B µg/g (1270)	B µg/g (4f)	Li µg/g	F µg/g	Cl µg/g	H$_2$O wt. %
Valle d'Aosta (DC47)											
OL	36_36-DC47-OL	642	1132	+ 18.0	±1.2	15.9	18.6	0.1	11.4	11.5	<d.l
OL	40_40-DC47-OL	111	6268	+ 18.6	±1.2	24.9	28.6	0.5	12.0	12.8	<d.l
OL	42_42-DC47-OL	649	6874	+ 17.1	±1.2	24.0	15.4	0.2	12.1	9.9	<d.l
OL	41_41-DC47-OL	1203	6754	+ 18.1	±1.1	24.0	16.8	0.3	11.0	8.6	<d.l
SRP	37_37-DC47-ATG	852	1286	+ 20.2	±1.3	12.7	7.4	<d.l	23.7	19.7	13.3
SRP	43_43-DC47-ATG	488	6154	+ 19.2	±1.3	9.6	16.7	<d.l	20.7	36.6	12.8
SRP	38_38-DC47-SRP	903	2662	+ 21.2	±1.4	9.0	n.a.	n.a.	n.a.	n.a.	n.a.
SRP	39_39-DC47-SRP	-144	4410	+ 20.3	±1.4	8.5	n.a.	n.a.	n.a.	n.a.	n.a.
Erro Tobbio (VT8-3)											
OL	3_VT8-3_ol1	-3586	-3568	+ 18.1	±1.5	12.2	17.4	3.6	12.9	270.0	0.1
OL	11_VT8-3_ol2	3949	2837	+ 18.8	±1.5	9.9	14.4	48.2	17.2	48.1	<d.l
OL	13_VT8-3_ol3	2540	5725	+ 19.9	±1.5	10.5	18.6	3.7	19.3	23.0	<d.l
OL	15_VT8-3_ol4	-5142	511	+ 19.7	±1.6	9.6	13.2	13.6	8.3	24.5	<d.l
SRP	5_VT8-3_atg1	-3505	-5183	+ 17.3	±1.7	8.6	13.6	0.1	590.0	41.8	14.1
SRP	8_VT8-3_atg2	3997	-2209	+ 16.4	±1.5	10.1	10.5	0.1	195.0	49.4	14.2
Monviso (Vis5b)											
OL	6_Vis5b-ol01	-90	-2137	+ 11.3	±1.4	13.5	12.6	0.3	6.8	11.0	<d.l
OL	5_Vis5b-ol04	22	-1250	+ 8.4	±1.4	16.0	n.a.	n.a.	n.a.	n.a.	n.a.
OL	3_Vis5b-ol02a	109	-2087	+ 11.2	±1.5	12.0	n.a.	n.a.	n.a.	n.a.	n.a.
OL	4_Vis5b-ol02	181	-2100	+ 9.6	±1.5	9.2	8	0.1	4.1	2.4	<d.l
OL	7_Vis5b-ol06	152	-1276	+ 11.7	±1.4	12.6	11.2	0.1	8.8	6.5	0.1
SRP	1_Vis5b-atg01	-426	-1510	+ 19.0	±1.8	5.3	1.8	<d.l	14.0	18.1	14.2
SRP	8_Vis5b-atg04	-327	-1477	+ 18.4	±2.1	2.5	1.6	<d.l	19.1	35.3	13.1
SRP	2_Vis5b-atg02	-717	-1180	+ 19.7	±1.7	5.8	2.9	<d.l	28.9	25.3	13.7
Monviso (DC84)											
OL	47_DC84-OL	-916	178	+ 13.0	±1.2	20.2	7.2	<d.l	10.2	5.7	<d.l
OL	53_DC84-OL	-237	-1398	+ 12.5	±1.2	16.6	21.7	0.1	27.4	13.2	<d.l
OL	48_DC84-X	-808	1772	+ 9.9	±1.3	14.9	n.a.	n.a.	n.a.	n.a.	n.a.
OL	54_DC84-OL	755	-1914	+ 14.1	±1.2	32.7	n.a.	n.a.	n.a.	n.a.	n.a.
OL	51_DC84-X	2111	3626	+ 11.7	±1.3	13.0	n.a.	n.a.	n.a.	n.a.	n.a.
SRP	49_DC84-SRP	649	1254	+ 20.3	±1.5	5.8	5	<d.l	12.2	13.9	12.6
SRP	55_DC84-SRP	1608	-2284	+ 20.0	±1.7	3.3	2.7	<d.l	16.6	18.0	12.7
SRP	52_DC84-SRP	-2188	1346	+ 19.2	±1.5	5.4	3.6	<d.l	17.1	16.5	12.2
SRP	50_DC84-SRP	1476	3526	+ 20.2	±1.4	9.1	7.1	<d.l	18.0	31.0	12.9
SRP	56_DC84-SRP	3123	-2232	+ 21.4	±1.4	9.9	7.4	<d.l	12.0	13.0	13.0

Table S-4   Representative major element analyses (wt %) of metamorphic olivine by EPMA.

Sample	SiO$_2$	TiO$_2$	Cr$_2$O$_3$	FeO	MnO	NiO	MgO	CaO	Total	Fo%
Val d'Aosta										
DC47	41.56	<d.l.	<d.l.	7.76	0.38	0.35	51.14	<d.l.	101.17	92.2
DC47	40.90	<d.l.	<d.l.	8.13	0.37	0.34	51.17	<d.l.	100.91	91.8
Zermatt										
ZS17-8	41.40	0.01	<d.l.	3.61	0.31	0.24	55.06	<d.l.	100.63	96.5
ZS17-8	42.41	0.01	<d.l.	5.04	0.31	0.29	53.75	<d.l.	101.81	95.0
ZS17-9	41.62	<d.l.	0.01	4.19	0.24	0.23	53.91	<d.l.	100.20	95.8
ZS17-9	41.00	<d.l.	<d.l.	4.29	0.23	0.26	54.50	<d.l.	100.28	95.8
ZS1	41.73	<d.l.	<d.l.	5.99	0.33	0.21	52.73	<d.l.	101.00	94.0
ZS1	41.55	<d.l.	0.01	6.23	0.23	0.27	52.34	0.01	100.64	93.7
ZS1	41.54	<d.l.	<d.l.	5.93	0.28	0.34	52.90	<d.l.	100.98	94.1
Monviso										
DC84	39.21	<d.l.	<d.l.	16.68	0.52	0.01	44.35	0.03	100.81	82.6
DC84	39.49	<d.l.	0.01	12.90	0.34	0.17	46.63	0.02	99.56	86.6
DC84	40.07	0.01	0.01	8.67	0.20	0.04	50.59	0.03	99.62	91.2
Vis5b	39.71	<d.l.	0.01	10.75	0.36	0.46	48.17	0.02	99.51	88.9
Vis5b	39.88	0.01	<d.l.	10.84	0.51	0.23	47.95	0.02	99.44	88.7
Erro-Tobbio										
VT8-3	40.03	<d.l.	<d.l.	12.60	0.35	0.32	46.82	0.01	100.19	86.9
VT8-3	39.26	0.86	0.05	12.13	0.29	0.30	46.71	0.01	100.47	87.3

<d.l. = less than detection limit (<0.01 for all elements). VT8-3 data from De Hoog *et al*. (2014).

Table S-5 Representative major element analyses (wt %) of serpentine by EPMA.

Sample	SiO$_2$	Al$_2$O$_3$	FeO	MgO	MnO	NiO	Cr$_2$O$_3$	Total	Mg#
Val d'Aosta									
DC47	43.43	2.09	2.79	39.31	0.04	0.12	0.27	88.05	96.2
DC47	44.19	1.20	2.64	39.61	0.07	0.11	0.25	88.08	96.4
DC47	43.73	1.73	2.66	39.92	0.04	0.10	0.15	88.33	96.4
Zermatt									
ZS17-8	42.54	2.11	2.16	40.19	0.03	0.07	0.42	87.52	97.1
ZS17-8	42.65	2.10	2.03	40.61	0.05	0.11	0.18	87.74	97.3
ZS17-8	43.08	1.99	1.85	40.51	0.03	0.09	0.24	87.80	97.5
ZS17-8	42.68	2.08	1.98	40.15	0.04	0.06	0.83	87.83	97.3
ZS17-9	42.40	1.84	1.92	39.59	0.03	0.10	0.60	86.48	97.4
ZS17-9	42.67	1.64	2.30	39.91	0.04	0.10	0.42	87.06	96.9
ZS17-9	42.97	2.20	2.27	39.25	0.04	0.11	0.46	87.32	96.8
ZS1	43.10	1.60	2.00	39.90	0.00	0.10	0.40	87.10	97.3
ZS1	42.10	1.80	2.10	39.30	0.10	0.10	0.60	86.00	97.1
ZS1	43.50	1.70	1.80	40.00	0.00	0.10	0.20	87.90	97.5
Monviso									
DC84	41.72	2.25	2.96	38.06	0.03	0.09	0.89	86.01	95.8
DC84	42.81	1.31	2.99	38.88	0.03	0.01	0.39	86.69	95.9
DC84	42.31	1.74	3.09	38.46	0.03	0.02	0.52	86.42	95.7
Vis5b	43.03	1.65	2.79	39.13	0.02	0.11	0.43	87.17	96.1
Vis5b	42.84	2.16	2.92	38.78	0.03	0.16	0.68	87.57	96.0
Vis5b	43.26	1.73	3.11	38.97	0.03	0.18	0.29	87.58	95.7
Erro-Tobbio									
VT8-3	41.54	2.56	3.66	37.00	0.05	0.07	0.11	85.02	94.7

VT8-3 data from De Hoog *et al*. (2014).

Table S-6 Representative major element analyses (wt %) of accessory silicate phases by EPMA, where present.

Sample	Phase	SiO_2	TiO_2	Al_2O_3	Cr_2O_3	FeO	MnO	NiO	MgO	CaO	Na_2O	Total
Zermatt												
ZS17-8	Chu	37.23	3.69	<0.01	0.01	4.52	0.34	0.20	52.32	<0.01	n.a.	98.31
ZS17-8	Cpx	55.17	<0.01	0.01	0.01	0.66	0.06	0.01	18.42	25.54	n.a.	99.89
ZS17-9	Chl	33.66	<0.01	11.71	1.54	3.34	0.02	0.13	35.21	<0.01	n.a.	85.63
Erro-Tobbio												
VT8-3	Chu	36.53	4.72	<0.01	0.08	13.02	0.44	0.20	44.13	<0.01	n.a.	99.12
VT8-3	Chu	32.69	7.76	0.01	0.12	12.71	0.44	0.14	42.64	<0.01	n.a.	96.52
VT8-3	Cpx	51.26	0.40	5.46	1.12	2.72	0.05	0.02	15.26	22.91	0.31	99.51
VT8-3	Cpx	54.46	0.01	0.05	0.02	1.91	0.10	<0.01	17.57	25.58	<0.02	99.70
VT8-3	Chl	37.60	0.05	8.66	1.06	3.69	<0.01	0.13	35.32	0.05	0.06	86.62

n.a. = not analysed, chu = clinohumite, chl = chlorite, cpx = clinopyroxene ; VT8-3 data from De Hoog *et al*. (2014).

Supplementary Information References

Amato, J.M., Johnson, C.M., Baumgartner, L.P., Beard, B.L. (1999) Rapid exhumation of the Zermatt-Saas ophiolite deduced from high-precision Sm-Nd and Rb-Sr geochronology. *Earth and Planetary Science Letters* 171, 425–438.

Angiboust, S., Langdon, R., Agard, P., Waters, D., Chopin, C. (2012) Eclogitization of the Monviso ophiolite (W. Alps) and implications on subduction dynamics. *Journal of Metamorphic Geology* 30, 37-61.

Angiboust, S., Pettke, T., De Hoog, J.C.M., Caron, B., Oncken, O. (2014) Channelized fluid flow and eclogite-facies metasomatism along the subduction shear zone. *Journal of Petrology* 55, 883–916, doi: 10.1093/petrology/egu010.

Barnicoat, A.C., Fry, N. (1986) High-pressure metamorphism of the Zermatt-Saas ophiolite zone, Switzerland. *Journal of the Geological Society 143*, 607–618.

Bell, D.R., Hervig, R.L., Buseck, P.R., Aulbach, S. (2009) Lithium isotope analysis of olivine by SIMS: Calibration of a matrix effect and application to magmatic phenocrysts. *Chemical Geology* 258, 5-16.

Cannaò, E., Scambelluri, M., Agostini, S., Tonarini, S., Godard, M. (2016) Linking serpentinite geochemistry with tectonic evolution at the subduction plate-interface: The Voltri Massif case study (Ligurian Western Alps, Italy). *Geochimica et Cosmochimica Acta* 190, 115–133, doi: 10.1016/j.gca.2016.06.034.

Capponi, G., Crispini, L. (2002) Structural and metamorphic signature of alpine tectonics in the Voltri Massif (Ligurian Alps, North - Western Italy). *Eclogae Geologicae Helvetiae* 95, 31–42.

Catanzaro, E.J., Champion, C.E., Garner, E.L., Marinenko, G., Sappenfield, K.M., Shields, W.R. (1970) Standard reference materials: boric acid; isotopic, and assay standard reference materials. *NBS Special Publication* 260, 1–70.

De Hoog, J.C.M., Gall, L., Cornell, D. (2010) Trace element geochemistry of mantle olivine and applications to mantle petrogenesis and geothermobarometry. *Chemical Geology* 270, 196–215.

De Hoog, J.C.M., Hattori, K., Jung, H. (2014) Titanium- and water-rich metamorphic olivine in high-pressure serpentinites from the Voltri Massif (Ligurian Alps, Italy): Evidence for deep subduction of high-field strength and fluid-mobile elements. *Contributions to Mineralogy and Petrology* 167, 1–15, doi: 10.1007/s00410-014-0990-x.

De Hoog, J.C.M., Monteleone, B.D., Savov, I, Marschall, H., Zack, T., EIMF (2017) Matrix effects in B isotope analysis of silicate minerals by SIMS, in *Goldschmidt Abstracts*, abstract 872.

Debret, B., Koga, K.T., Nicollet, C., Andreani, M., Schwartz, S. (2013) F, Cl and S input via serpentinite in subduction zones: implications for the nature of the fluid released at depth. *Terra Nova* 26, 96–101, doi: 10.1111/ter.12074.

Debret, B., Sverjensky, D.A. (2017) Highly oxidising fluids generated during serpentinite breakdown in subduction zones. Scientific Reports 7.

Galvez, M.E., Connolly, J.A.D., Manning, C.E. (2016) Implications for metal and volatile cycles from the pH of subduction zone fluids. Nature 539, 420-424.

Gilio, M., Scambelluri, M., Agostini, S., Godard, M., Peters, D., Pettke, T. (2019) Petrology and geochemistry of serpentinites associated with the ultra-high pressure Lago di Cignana Unit (Italian Western Alps). *Journal of Petrology* 60, 1229-1262.

Gilio, M., Scambelluri, M., Agostini, S., Godard, M., Pettke, T., Agard, P., Locatelli, M., Angiboust, S. (2020) Fingerprinting and relocating tectonic slices along the plate interface: Evidence from the Lago Superiore unit at Monviso (Western Alps). *Lithos* 352.

Groppo, C., Castelli, D. (2010) Prograde P - T Evolution of a Lawsonite Eclogite from the Monviso Meta-ophiolite (Western Alps): Dehydration and Redox Reactions during Subduction of Oceanic FeTi-oxide Gabbro. *Journal of Petrology* 51, 2489–2514, doi: 10.1093/petrology/egq065.

Guillot, S., Schwartz, S., Hattori, K., Auzende, A., Lardeaux, J. (2004) The Monviso ophiolitic massif (Western Alps), a section through a serpentinite subduction channel. *Journal of the Virtual Explorer* 16, <hal-00103165>.

Healy, D., Reddy, S.M., Gray, E.M., Brovarone, A.V., Timms, N.E. (2009) Trench-parallel fast axes of seismic anisotropy due to fluid-filled cracks in subducting slabs. *Earth and Planetary Science Letters* 283, 75–86, doi: 10.1016/j.epsl.2009.03.037.

Jochum, K.P., Dingwell, D.B., Rocholl, A., Stoll, B., Hofmann, A.W., Becker, S., Besmehn, A., Besserte, D., Dietze, H.J., Dulski, P., Erzinger, J., Hellebrand, E., Hoppe, P., Horn, I., *et al.* (2000) The preparation and preliminary characterisation of eight geological MPI-DING reference glasses for in-situ microanalysis. *Geostandards Newsletter* 24, 87–133, doi: 10.1111/j.1751-908X.2000.tb00590.x.

Jochum, K.P., Nohl, U., Herwig, K., Lammel, E., Stoll, B., Hofmann, A.W. (2005) GeoReM: A New Geochemical Database for Reference Materials and Isotopic Standards. *Geostandards and Geoanalytical Research* 29, 333–338, doi: 10.1111/j.1751-908x.2005.tb00904.x.

Kempf, E.D., Hermann, J. (2018) Hydrogen incorporation and retention in metamorphic olivine during subduction: Implications for the deep water cycle. *Geology* 46, 571-574.

Kretz, R. (1983) Symbols for rock-forming minerals. *American Mineralogist* 68, 277–279.

Lesne, P., Kohn, S.C., Blundy, J., Witham, F., Botcharnikov, R.E., Behrens, H. (2011) Experimental simulation of closed-system degassing in the system basalt-H_2O-CO_2-S-Cl. *Journal of Petrology* 52, 1737–1762, doi: 10.1093/petrology/egr027.

Li, X.., Rahn, M., Bucher, K. (2004) Serpentinites of the Zermatt-Saas ophiolite complex and their texture evolution. *Journal of Metamorphic Geolog*y 22, 159–177, doi: 10.1111/j.1525-1314.2004.00503.x.

López Sánchez-Vizcaíno, V., Gómez-Pugnaire, M.T., Garrido, C.J., Padrón-Navarta, J.A., Mellini, M. (2009) Breakdown mechanisms of titanclinohumite in antigorite serpentinite (Cerro del Almirez massif, S. Spain): A petrological and TEM study. *Lithos* 107, 216–226, doi: 10.1016/j.lithos.2008.10.008.

Marschall, H.R., Monteleone, B.D. (2015) Boron Isotope Analysis of Silicate Glass with Very Low Boron Concentrations by Secondary Ion Mass Spectrometry. *Geostandards and Geoanalytical Research* 39, 31-46.

Martin, S., Rebay, G., Kienast, J.R., Mével, C. (2008) An eclogitised oceanic palaeo-hydrothermal field from the St. Marcel Valley (Italian Western Alps). *Ofioliti* 33, 49-63.

Mattia G., Scambelluri, M., Agostini, S., Godard, M., Peters, D., Pettke, T. (2019) Petrology and Geochemistry of Serpentinites Associated with the Ultra-High Pressure Lago di Cignana Unit (Italian Western Alps). *Journal of Petr*ology 60, 1229–1262, doi: 10.1093/petrology/egz030.

Pabst, S., Zack, T., Savov, I.P., Ludwig, T., Rost, D., Tonarini, S., Vicenzi, E.P. (2012) The fate of subducted oceanic slabs in the shallow mantle: insights from boron isotopes and light element composition of metasomatized blueschists from the Mariana forearc. *Lithos* 132-133, 162-179.

Rebay, G., Spalla, M. Zanoni, D. (2012) Interaction of deformation and metamorphism during subduction and exhumation of hydrated oceanic mantle: insights from the Western Alps. *Journal of Metamorphic Geology* 30, 687–702.

Rouméjon, S., Cannat, M. (2014) Serpentinization of mantle-derived peridotites at mid-ocean ridges: Mesh texture development in the context of tectonic exhumation. *Geochemistry, Geophysics, Geosystems* 15, 2354-2379, doi: 10.1002/2013GC005148

Rubatto, D., Angiboust, S. (2015) Oxygen isotope record of oceanic and high - pressure metasomatism : a P – T – time – fluid path for the Monviso eclogites (Italy). *Contributions to Mineralogy and Petrology* 170, 1–16, doi: 10.1007/s00410-015-1198-4.

Rubatto, D., Herman, J. (2003) Zircon formation during fluid circulation in eclogites (Monviso, Western Alps): Implications for Zr and Hf budget in subduction zones. *Geochimica et Cosmochimica Acta* 67, 2173–2187, doi: 10.1016/S0016-7037(02)01321-2.

Scambelluri, M., Hoogerduijn Strating, E.H., Piccardo, G.B., Vissers, R.L.M., Rampone, E. (1991) Alpine olivine- and titanian clinohumite-bearing assemblages in the Erro-Tobbio peridotite (Voltri Massif, NW Italy). *Journal of Metamorphic Geology* 9, 79–91, doi: 10.1111/j.1525-1314.1991.tb00505.x.

Scambelluri, M., Muntener, O., Hermann, J., Piccardo, G.B., Trommsdorff, V. (1995) Subduction of water into the mantle - history of an alpine peridotite. *Geology* 23, 459–462, doi: 10.1130/0091-7613(1995)023.

Scambelluri, M., Muntener, O., Ottolini, L., Pettke, T.T., Vannucci, R. (2004) The fate of B , Cl and Li in the subducted oceanic mantle and in the antigorite breakdown fluids. *Earth and Planetary Science Letters* 222, 217–234, doi: 10.1016/j.epsl.2004.02.012.

Scambelluri, M., Tonarini, S. (2012) Boron isotope evidence for shallow fluid transfer across subduction zones by serpentinized mantle. *Geology* 40, 907–910, doi: 10.1130/G33233.1.

Tartarotti, P., Martin, S., Polino, R. (1986) Geological data about the ophiolitic sequences in the St. Marcel Valley (Aosta Valley). *Ofioliti* 11 (3), 343-346.

Tenthorey, E., Herman, J. (2004) Composition of fluids during serpentinite breakdown in subduction zones: Evidence for limited boron mobility. *Geology* 32, no. 10, 865–868, doi: 10.1130/G20610.1.

Tonarini, S., Leeman, W.P., Leat, P.T. (2011) Subduction erosion of forearc mantle wedge implicated in the genesis of the South Sandwich Island (SSI) arc: Evidence from boron isotope systematics. *Earth and Planetary Science Letters* 301, 275–284, doi: 10.1016/j.epsl.2010.11.008.

Walowski, K. J., L. A. Kirstein, J. C. M. De Hoog, T. R. Elliott, I. P. Savov, R. E. Jones, EIMF (2019) Investigating ocean island mantle source heterogeneity with boron isotopes in melt inclusions. *Earth and Planetary Science Letters* 508, 97-108.

Whitney, D.L., Evans, B.W. (2010) Abbreviations for names of rock-forming minerals. *American Mineralogist* 95, 185–187, doi: 10.2138/am.2010.3371.

Williams, L.B., Hervig, R.L., Holloway, J.R., Hutcheon, I. (2001) Boron isotope geochemistry during diagenesis. Part I. Experimental determination of fractionation during illitization of smectite. *Geochimica et Cosmochimica Acta* 65, 1769–1782.

Yamada, C., Tsujimori, T., Chang, Q., Kimura, J.I. (2019) Boron isotope variations of Franciscan serpentinites, northern. California. *Lithos* 334, 180-189.